

Core-collapse supernovae ages and metallicities from emission-line diagnostics of nearby stellar populations

Lin Xiao^{1,2,3★}, L. Galbany,⁴ J. J. Eldridge³ and Elizabeth R. Stanway⁵

¹CAS Key Laboratory for Research in Galaxies and Cosmology, Department of Astronomy, University of Science and Technology of China, Hefei, 230026, China

²School of Astronomy and Space Sciences, University of Science and Technology of China, Hefei 230026, China

³Department of Physics, University of Auckland, NZ

⁴PITT PACC, Department of Physics and Astronomy, University of Pittsburgh, Pittsburgh, PA 15260, USA

⁵Department of Physics, University of Warwick, Gibbet Hill Road, Coventry, CV4 7AL

Accepted 2018 September 13. Received 2018 September 13; in original form 2018 May 3

ABSTRACT

Massive stars are the main objects that illuminate H II regions and they evolve quickly to end their lives in core-collapse supernovae (CCSNe). Thus, it is important to investigate the association between CCSNe and H II regions. In this paper, we present emission-line diagnostics of the stellar populations around nearby CCSNe, which include their host H II regions, from the Potsdam Multi-Aperture Spectrophotometer (PMAS)/PPak integral-field supernova hosts compilation (PISCO). We then use BPASS stellar population models to determine the age, metallicity and gas parameters for H II regions associated with CCSNe, contrasting models that either consider single-star evolution alone or incorporate interacting binaries. We find that binary-star models, which allow for ionizing photon loss, provide a more realistic fit to the observed CCSN hosts, with metallicities that are closer to those derived from the oxygen abundance in O3N2. We also find that Type II and Type Ibc SNe arise from progenitor stars of similar age, mostly from 7 to 45 Myr, which corresponds to stars with masses $\leq 20 M_{\odot}$. However, these two types of SNe have little variations in their host environment metallicity measured by oxygen abundance or in progenitor initial mass. We note that at lower metallicities the SNe are more likely to be Type II.

Key words: binaries: general – supernovae: general – H II regions – galaxies: general.

1 INTRODUCTION

Core-collapse supernovae (CCSNe) originate in massive stars ($\geq 8 M_{\odot}$), as a result of the gravitational collapse of the iron-group element cores that are the final result of their core nuclear burning. Given their short lifetimes, these massive CCSN progenitors tend to be associated with their birth place (star clusters or H II regions) with only a low possibility of being ejected from their birth place due to dynamical interactions or supernova kicks (De Donder & Vanbeveren 1997; de Wit et al. 2005; Eldridge, Langer & Tout 2011; Renzo et al. 2018). With direct detections of CCSN progenitor stars remaining rare (Smartt 2015), the study of their environment represents a good alternative to put constraints on their characteristics (e.g. Williams et al. 2014, 2018; Zapartas et al. 2017).

Here, we focus on the emission-line nebulae, or H II regions, associated with CCSNe. Previous studies of CCSN locations within their host galaxies have claimed various associations with H II re-

gions. Based on a sample of 38 CCSNe of all subtypes, van Dyk (1992) undertook the first attempt to assess the CCSNe association with H II regions, and concluded that approximately 50 per cent were associated with an H II region, with no statistically significant difference between Type II (hydrogen-rich) and Type Ibc (stripped-envelope) CCSNe. More recently, Anderson & James (2008) found a low fraction of SNe II to be associated with H II regions while SNe Ibc are spatially coincident with them. This has led to an interpretation that the progenitors of SNe Ibc are more massive than those of SNe II. Crowther (2013) examined the immediate environments of 39 CCSNe in nearby galaxies and obtained similar results to Anderson & James (2008). However, Crowther argued that the observed association between certain CCSNe and H II regions provides only weak constraints upon their progenitor masses because the H II regions of these CCSN hosts are long-lived giant H II regions (~ 20 Myr) rather than short-lived (~ 4 Myr) isolated, compact H II regions where most star formation occurs.

Other studies (e.g. Williams et al. 2014, 2018) have instead focused on the surrounding stellar populations of CCSNe. By studying the resolved stellar population around the site of a CCSN and

* E-mail: lxiao33@ustc.edu.cn

assuming that the age is similar to that of the progenitor, ages from a few Myr up to a few 10 Myr have been found, in agreement with the range of ages possible for SNe from theoretical predictions (e.g. Zapartas et al. 2017). Therefore, the ages and progenitor masses also agree with those for the directly detected SN progenitors (Smartt 2015).

In addition to estimating the age of a SN progenitor, it is also important to estimate its metallicity. The gas-phase metallicity can be estimated for the CCSN host environment from emission-line diagnostics. To accurately explain the differences in observed CCSN progenitors, we must understand both their ages and metallicities. Prantzos & Boissier (2003) used the metallicity–luminosity relation for late-type galaxies and found that the observed ratio of SNe Ibc to SNe II depended strongly on the metallicity of the host galaxy. In those more luminous and metal-rich galaxies, higher ratios of SNe Ibc to SNe II are expected. Similar results for the dependence of the relative ratio of SN subtypes on metallicity have been obtained by many authors, including, for example, Prieto, Stanek & Beacom (2008) and Graur et al. (2017). We note that stellar evolution theory suggests that this relationship between the ratio of SN types and metallicity can provide important constraints on how important stellar rotation and binary interactions are in the evolution of progenitor stars (e.g. Podsiadlowski et al. 1992; De Donder & Vanbeveren 1998; Heger et al. 2003; Maeder & Meynet 2004; Eldridge, Izzard & Tout 2008; Zapartas et al. 2017).

Recently, integral field spectroscopy (IFS) has begun to enable larger-scale investigations over both spatial and spectral dimensions to investigate SN environments and active star-forming regions. For example, Kuncarayakti et al. (2013a,b) used small-field (6×6 arcsec²) IFS observations to identify single stellar clusters that had hosted CCSNe. They estimated their metallicities from the measured emission lines via strong-line methods, and their ages by comparing the H α emission equivalent width with simple stellar population models. They were able to estimate both the metallicity and initial mass of the CCSN progenitor stars. They concluded that, on average, SNe Ibc explosion sites are more metal-rich than SNe II sites, and that some SNe II progenitors might have been stars with masses comparable to those of SNe Ibc progenitors.

Another advantage of IFS is that it enables simultaneous investigations of the overall properties of the host galaxy and its spatially resolved structure. This allows more constraints on the nature of the progenitors of different SN types, by looking for differences in local environmental parameters, as well as relating them to the overall distribution across the galaxy extent, as shown by Galbany et al. (2014, 2016b). These authors constructed statistical samples to compare the star formation density and metallicity of stars at the locations of different SN types and they confirmed that SNe Ibc show the closest relation to star-forming regions and are more associated with metal-rich environments than SNe II. Similar results have been found in other recent studies based on different observed samples, such as studies of SN explosion sites using the Multi-Unit Spectroscopic Explorer (MUSE) IFS (Galbany et al. 2016a; Kuncarayakti et al. 2017) and the Potsdam Multi-Aperture Spectrophotometer (PMAS)/PPak integral-field supernova hosts compilation (PISCO), which is the largest updated sample of SN host galaxies observed with IFS, and consists of 272 SNe including 152 CCSNe (Galbany et al. 2018).

However, all the above IFS studies assume one (mostly unstated) caveat, which is that they all assume that stars evolve in isolation as single stars. In fact, over 70 per cent of massive stars are found in binary or multiple systems (e.g. Sana et al. 2012, 2014). Binary interactions cause mass transfer between stars, leading to new

evolution pathways with respect to single-star evolution, and they substantially change the appearance of stellar populations (e.g. Eldridge et al. 2017; Xiao, Stanway & Eldridge 2018). In this work, we aim to investigate the effect of interacting binaries on SNe and the emission lines from the nearby host stellar populations. We then constrain the ages and metallicities of the CCSN progenitor population, taking full account of interacting binary stars.

To achieve our main aim of exploring the effects of binary evolution on the nature of CCSN progenitor stars and their host environment, we use the latest BPASS (binary population spectral and synthesis) models v2.1 (Eldridge et al. 2017) and our nebular emission-line models that have previously been discussed in Xiao et al. (2018). Using these, we derive the properties of the underlying stellar population from the best-fitting models that match each individual H II region.

This paper is organized as follows. In Section 2, we describe the characteristics of the observed sample of H II regions with CCSN hosts from PISCO, we highlight some important observation quantities and we discuss the photoionization map behaviour of these CCSN hosts. Then, in Section 3, we briefly explain our numerical method for nebular emission models and the selection of best-fitting models, which is discussed in more detail in Xiao et al. (2018). In Section 4, we describe the best-fitting models in terms of their oxygen abundance, comparing with observed values and other physical parameters that determine the H II region models. In Section 5, we include the effect of ionizing photon leakage on best-fitting models and we describe the results in the leakage case compared with the cases without leakage. In Section 6, we present further discussions on the uncertainties of our model and result. Finally, in Section 7, we summarize and give our conclusions.

2 SAMPLE OF CCSN HOST H II REGIONS AND DATA SET ANALYSIS

2.1 Overview of the sample

The sample of H II regions with CCSN hosts used in this work comes from PISCO (Galbany et al. 2018), which started as an extension of the Calar Alto Legacy Integral Field Area (CALIFA) survey targeting low-mass SN host galaxies that were missing in the CALIFA mother sample. So, the instrumental configuration, observations and reduction are performed following CALIFA procedures and reduction pipeline. All of this information is well established and is available in Galbany et al. (2018) and references therein, as well as in the third CALIFA data release (Sánchez et al. 2016, and reference therein), including sky subtraction and flux calibration. Overall, the sample is comprised of observations of CCSN host galaxies selected from the CALIFA survey and other dedicated programmes using the PMAS/PPak integral field unit with large field of view ($\sim 1 \times 1$ arcmin²). The SN position was determined from the astrometry of the PISCO/CALIFA data cubes, and the aperture extraction was centred at that location. We required emission lines to have a signal-to-noise ratio (S/N) > 3 in order to be considered reliable, although in practice all have S/N > 5. The spectral information covers most of the optical domain from 3750 to 7300 Å, with a spectral resolution ranging from ~ 2.7 Å in the blue to ~ 6 Å in the red.

The observational sample we use consists of 152 CCSNe with 107 SNe II and 45 SNe Ibc, and their observed flux is derived within 1kpc² centred at the SN location. This is to provide us with adequate S/N in our spectra, while limiting the observation to the likely host stellar population around the SN site and preventing the

varying distance to the host galaxy from causing artefacts in our analysis. Extragalactic H II regions as well as H II clumps with SN hosts have typical diameters $\sim 10\text{--}100$ pc but range up to several hundred parsec with the expansion of H II regions driven by nuclear activities and stellar feedback (Gonzalez Delgado & Perez 1997; Lopez et al. 2011). This implies that between one and six H II regions are included in a 1 kpc^2 box (Mast et al. 2014), with relatively little dilution of the host region emission by unassociated nebular gas. Any contamination that is present will tend to be dominated by the youngest stellar population in the region and so bias CCSN host estimates to younger ages. The physical spatial resolution in the PISCO data set is presented in fig. 2 of Galbany et al. (2018). The average resolution of CCSN host observations in this work is $300\text{ pc arcsec}^{-1}$, so on average we integrated the spectra within the area covered by 3×3 spaxels (spatial pixels introduced by Kissler-patig et al. 2004). Only complete spaxels are included (i.e. no correction is made for partial spaxels). Furthermore, we have investigated the use of different definitions for the ‘nearby host stellar populations’, including the use of emission-line strengths from the nearest H II region and from 1 arcsec^2 around the SN location. We find that this choice does not affect our results to a large degree, as shown in Appendix B. Again, using the observed flux within 1 kpc^2 allows fair comparisons among SN local environments because the region compared does not vary in each galaxy. If an angular size were used, then the region integrated would vary as the area would vary with the redshift of each galaxy.

We also notice that all regions of these CCSN hosts have H α and [N II] $\lambda 6583$ emission while some might lack other emission lines, for example, one of 152 CCSN hosts without H β lines (SN 1989R), nine of 152 hosts without [O III] $\lambda 5007$, eight of 152 hosts without [S II] $\lambda 6713$ and 24 of 152 hosts without [O I] $\lambda 6300$. However, none of the hosts loses all four of these lines, and most lose only one emission line. Failure to detect individual emission lines usually indicates either that the line was coincident with sky emission or absorption features, or that nebular emission from the host region is weak, and might be dominated by the underlying stellar population rather than the host environment. While, in principle, this means that our survey might be biased against older H II regions, the effects on the distributions discussed in this paper are likely to be small. Approximately 20 per cent of Type II CCSN locations identified in PISCO, and 15 per cent of Type Ibc regions, have at least one line undetected, but for the bulk of the population only one line is missing. As a result, while older populations might be missed, again potentially biasing the sample to younger ages, the nebular regions should be indicative of the range of properties in the CCSNe progenitor stellar population.

2.2 Oxygen abundance

As in many previous studies, we derive the gas-phase metallicity of the H II regions in CCSN hosts from their measured fluxes via the strong-line method. This method is strongly affected by the choice of which strong-line abundance calibrations are used, as discussed in Kewley & Ellison (2008) and Xiao et al. (2018). In this work, we use the most widely used empirical O3N2 calibrator as our standard metallicity calibration, which is updated by Marino et al. (2013) using a new direct abundance measurement (T_e -based) provided by Pilyugin, Vílchez & Thuan (2010):

$$\text{O3N2} = \log([\text{O III}]\lambda 5007/\text{H}\beta)/([\text{N II}]\lambda 6583/\text{H}\alpha), \quad (1)$$

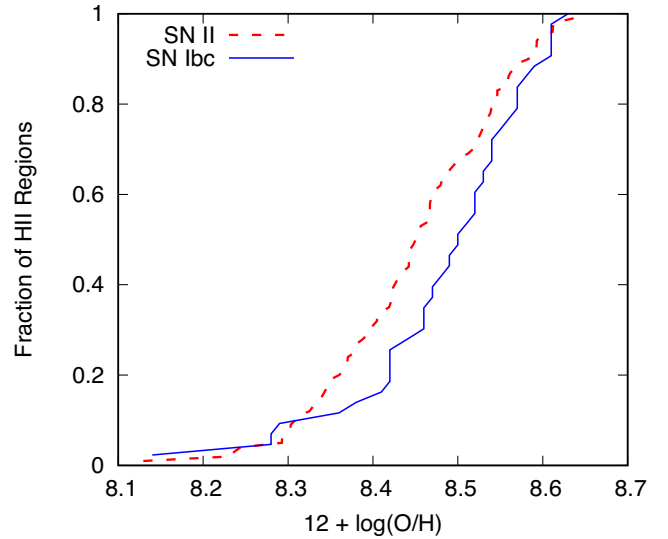


Figure 1. Cumulative distributions of the oxygen abundance of the H II regions in CCSN hosts. The red dashed line is for SNe II hosts and the blue solid line is for SNe Ibc hosts.

Table 1. The average value of oxygen abundance derived by the strong-line method described in Section 2.2 and the average emission-line ratios of the H II regions in CCSN hosts.

	SN II	SN Ibc
$12 + \log(\text{O}/\text{H})$	8.45 ± 0.10	8.49 ± 0.10
$\text{EW}(\text{H}\alpha)/\text{\AA}$	50.9 ± 49.1	49.9 ± 42.0
$\log([\text{O III}]/\text{H}\beta)$	-0.19 ± 0.32	-0.29 ± 0.33
$\log([\text{N II}]/\text{H}\alpha)$	-0.53 ± 0.22	-0.50 ± 0.20
$\log(\text{S II}/\text{H}\alpha)$	-0.45 ± 0.13	-0.51 ± 0.11
$\log(\text{O I}/\text{H}\alpha)$	-1.28 ± 0.25	-1.45 ± 0.19

$$12 + \log(\text{O}/\text{H}) = 8.533 - 0.214 \times \text{O3N2}. \quad (2)$$

The new calibration was tested by comparing with the measured oxygen abundance of 3423 observed CALIFA H II regions using the multiple line-ratio calibrations (Pilyugin et al. 2010). This improved O3N2 calibration shows weaker metallicity dependence and a relatively high precision with respect to other abundance determinations. This method was used by Galbany et al. (2016a) and Kuncarayakti et al. (2017) with MUSE data for the emission-line diagnostics of 11 and 83 H II regions in SN hosts, respectively.

Fig. 1 demonstrates the cumulative distribution of the oxygen abundances of SNe II and Ibc separately. The results indicate that these two types of CCSNe span a similar oxygen abundance range from 8.1 to 8.7 and the main fraction (about 80 per cent) is located in oxygen abundance from 8.3 to 8.6. Because of the steeper increasing trend of SNe Ibc, their overall metallicity is higher than that of SNe II. This result is reflected in their average oxygen abundance given in Table 1. SNe Ibc have an average of 8.49, slightly higher than SNe II with an average of 8.45.

2.3 Equivalent width of H α

The H α line luminosity is widely used to measure the amount of ongoing star formation. The H α equivalent width (EW), the measure of the relative strength of the line with respect to the continuum, is

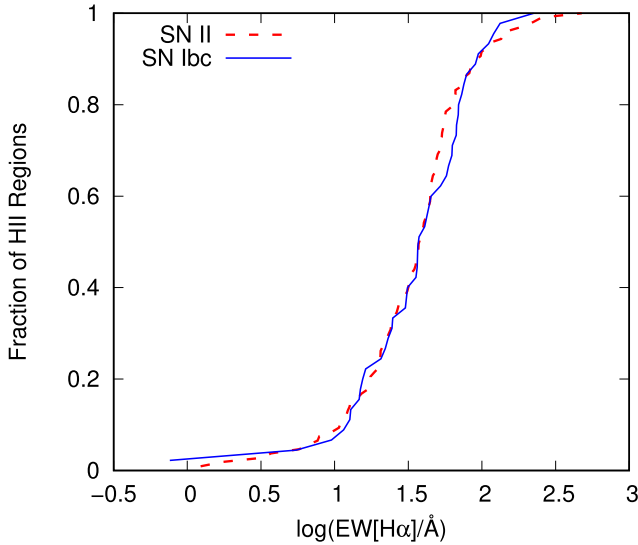


Figure 2. The cumulative distribution of H II regions in CCSN hosts as a function of H α EW with SNe II denoted by the red dashed line and SNe Ibc by the blue solid line.

commonly used to infer the age of a starburst. This is reasonable as the strength of this particular line is largely dependent on the ionizing condition of emission nebulae, which is dominated by the short-lived massive stars, and the continuum light is dominated by the long-lived lower-mass stars. Thus, the H α EW varies with the age and star formation history of the galaxy.

Fig. 2 shows the cumulative distribution of H α EW for our sample of SN hosts, where the two types of SN host have a similar distribution, with nearly 90 per cent of SNe having H α EW below 100 Å and above 8 Å, which indicates that most regions of SN hosts have significant hydrogen recombination lines from the nearby stellar populations. The similarity of these distributions is also shown by their almost identical mean H α EW, as seen in Table 1. Surprisingly, a SN II host has the highest H α EW of up to 400 Å, compared with that of the SNe Ibc of 250 Å. There could be many reasons for this, but it does indicate that although the EW is a useful estimator, there are many factors that limit its accuracy when studying the age of SN progenitors.

An important question in this study is whether the SNe are associated with a H II region or not. The H α EW distribution also allows us consider this question. The typical H α EW of a H II region varies but we see in our sample that there is a smooth distribution down to a EW of about 10 Å below which the distribution flattens out. This is perhaps indicative that all stellar populations have some associated nebular emission but only the brightest and most luminous are identified as H II regions. We do not attempt to determine the dividing line. If, for example, we were to say a EW of 100 Å and above indicated a H II region, then very few of our SNe would be associated with such a region. Most of our SNe are associated with nebular emission that is typically a few times 10 Å in strength.

In addition, we have tested how interacting binaries might affect the accuracy of age estimates using the H α EW. To do this, we use BPASS models v2.1 emission nebulae models (Eldridge et al. 2017; Xiao et al. 2018) to calculate the H α EW as a function of age and metallicity using only single stars or binary stars in the stellar population forming the ionizing source, as shown in Fig. 3. We assume a constant hydrogen density of $\log(n_H) = 2.0 \text{ cm}^{-3}$ and ionization parameter $\log(U) = -2.5$.

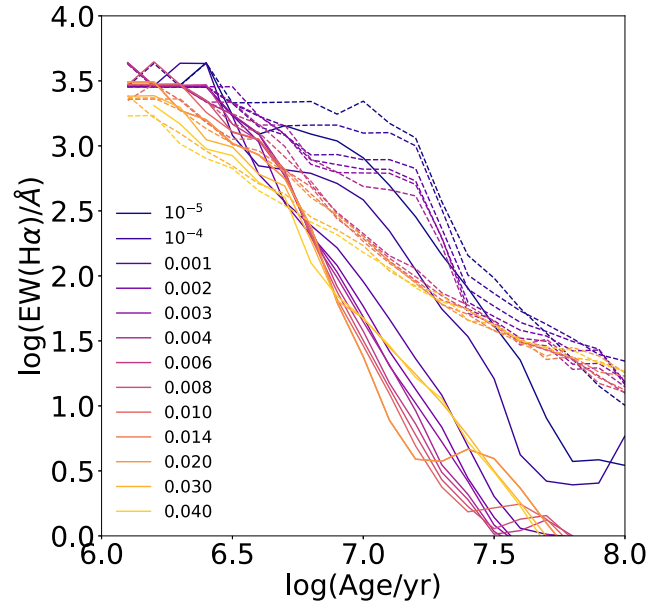


Figure 3. H α EW as a function of age at $\log(n_H) = 2.0 \text{ cm}^{-3}$ and $\log(U) = -2.5$ for both single-star (solid lines) and binary-star models (dashed lines) at increasing metallicities represented from blue to yellow.

For the first 3 Myr, both single-star and binary-star models have a high value of H α EW around 3000 Å. After this, the H α EW of single-star models experiences an abrupt decrease to less than 1 Å in 30 Myr. In contrast, the H α EW of binary-star models has a slower decline and is around 30 Å at the same age. This is because binary interactions strongly enhance the emission-line strength at ages beyond 10 Myr, producing a clear difference from single stars, due to the hot Wolf–Rayet or helium stars produced at later times via binary interactions (e.g. Van Bever et al., 1999; Götzberg, de Mink & Groh 2017; Xiao et al. 2018).

The H α EW is also strongly affected by metallicity as the main-sequence lifetime of massive stars is slightly increased at lower metallicity and stars are more compact and thus hotter. This means that the EW of low-metallicity models decreases more slowly than at higher metallicity. In addition, binary-star models naturally separate into two groups: a low-metallicity group of $Z \leq 0.004$ with a long plateau phase up to 20 Myr and high-metallicity group of $Z \geq 0.006$ with a gradual decrease without the plateau. The plateau is due to the inclusion of quasi-homogeneous evolution in low-metallicity binary-star systems where mass transfer has occurred. For stars with metallicities $Z \leq 0.004$ and initial masses above $20 M_\odot$ that accrete more than 5 per cent of their initial mass, we assumed that they were spun up so rapidly that they evolve fully mixed over their main-sequence lifetimes. This is discussed in detail in Eldridge et al. (2011, 2017). The mixing significantly extends the lifetime of massive stars in lower-metallicity models and they avoid a cool red supergiant phase and thus emit more ionizing photons than they would otherwise. In contrast, at metallicities above $Z > 0.004$, the H α EW is only weakly dependent on metallicity. Thus, given the moderate metallicities of our sample as shown in Fig. 1, the shape of our observed sample distribution in Fig. 2 is not strongly affected by metallicity.

Using our BPASS EW–age relationship and the metallicity derived using O3N2 calibration, we estimate the age separately for SNe II and Ibc from H α , as shown in Fig. 4. As the H α EW decreases with increasing age, we are able simply to estimate the age for

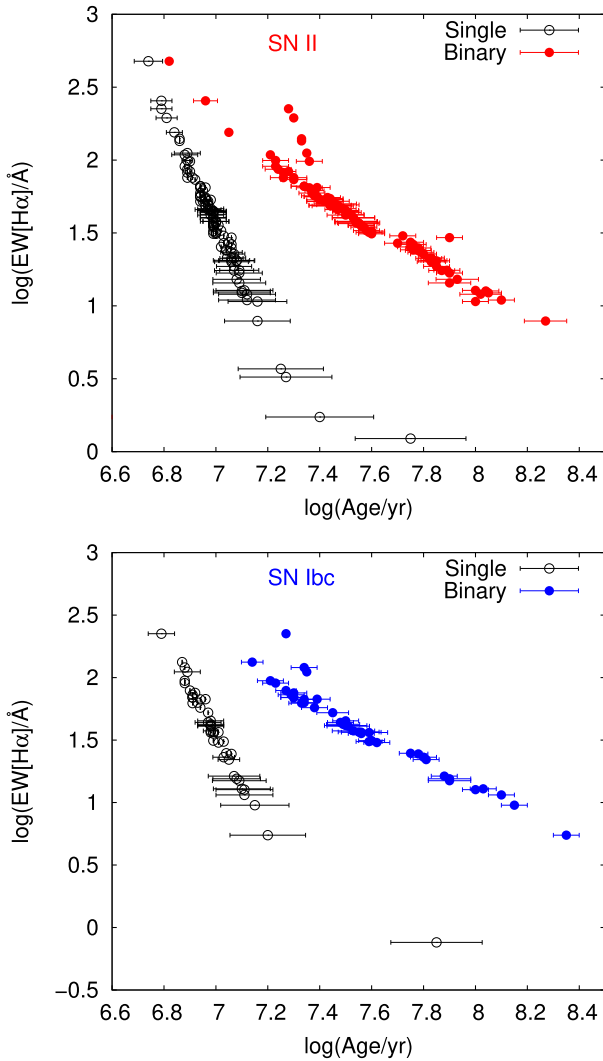


Figure 4. The distribution of $H\alpha$ EW with respect to age for SNe II (top panel) and SNe Ibc (bottom panel), assuming the simple relations described in Section 2.3. The black circles with error bars are for single-star models and red (SN II) and blue (SN Ibc) dots with error bars denote binary-star models. The errors are due to the uncertainty of observed $H\alpha$ EW values and the variance of the ionization parameter from $\log(U) = -3.5$ to -1.5 , at $\log(n_H) = 2.0 \text{ cm}^{-3}$.

all SN hosts. Using only our single-star models, most SNe have a progenitor age ≤ 20 Myr, while using the binary-star models leads to most ages being above this maximum, with ages up to 200 Myr being possible. We can conclude that binary interactions can significantly extend CCSN progenitor ages estimated from the $H\alpha$ EW. However, even when using the interacting binary-star models, we note that this method of estimating the age is highly uncertain because of the large scatter in the metallicity calibration, the sensitivity of the line strength to assumed metallicity and the uncertainties associated with the assumed binary fraction. Therefore, this age estimation should only be considered as an upper limit ($\gtrsim 50$ Myr) because there are no Galactic nebular regions against which we have calibrated and verified models of such extreme ages although we have performed some validation of such old models in Xiao et al. (2018). In addition, considering a CCSNe host in an old and diffused environment, the underlying stellar populations can contribute more to the measured $H\alpha$ EW than the emission nebulae. Therefore, these estimated ages

can be longer than the typical lifetime of H II regions (up to a few 10 Myr), and this is consistent with the CCSN ages of Hakobyan et al. (2017) using a completely different approach based on the CCSN spatial distribution in their host galaxies. However, in the real galaxies, planetary nebulae and other sources from X-ray binaries (Woods & Gilfanov 2016) can reach these late ages that are not yet in BPASS models.

2.4 Distribution of CCSN hosts in BPT diagrams

As in Xiao et al. (2018), we use the BPT diagrams first proposed by Baldwin, Phillips & Terlevich (1981) to study the ionizing conditions of these CCSN host stellar populations and thus to refine our estimates of age and metallicity. The distributions of the emission lines from the CCSN host stellar population are depicted in Fig. 5. We compare these with the H II regions taken from van Zee et al. (1998) and van Zee & Haynes (2006). These were H II regions identified in nearby galaxies.

The majority of sources in both the van Zee sample of galaxy H II regions and our sample of H II regions of CCSN hosts lie beneath the maximum theoretical starburst lines defined by Kewley et al. (2001), although there is some scatter above these lines, particularly in the [S II]- and [O I]-based diagnostics. The two samples do differ significantly with the H II regions of dwarf galaxies occupying the upper-left region in the BPT diagram. The CCSN hosts are mostly in the lower right of the diagram indicating they are diffuse, older nebula emission regions, without many stars hot enough to provide higher [O III] to $H\beta$ ratios. In addition, the CCSN hosts in the [O I]/ $H\alpha$ panel are more scattered left over the Kewley curve. SNe II regions are more likely to exceed the limiting Kewley relation in [O I]/ $H\alpha$ than SNe Ibc hosts. Aside from this, the range of line ratios spanned by the two samples is very similar. They form a narrow sequence in the map of [O III]/ $H\beta$ with [N II]/ $H\alpha$ as well as the [S II]/ $H\alpha$ diagram. Even though these hosts are dispersed across the map of [O III]/ $H\beta$ with [O I]/ $H\alpha$, SNe II hosts and SNe Ibc hosts still occupy nearly the same regions. These similar behaviours of SN hosts in BPT diagrams can also be reflected from their similar mean emission-line ratios as listed in Table 1, where SNe Ibc have slightly lower ratios in $\log([O III]/H\beta)$, $\log([S II]/H\alpha)$ and $\log([O I]/H\alpha)$, but a higher ratio of $\log([N II]/H\alpha)$.

3 METHOD

To model the nebular emission from stellar populations, we follow the methods described in Xiao et al. (2018). To briefly summarize our method, we use the latest BPASS models¹ v2.1 (Eldridge et al. 2017) to obtain the input ionizing spectra for CLOUDY 13.03 (Ferland et al. 1998, 2013) nebular models. We then use the CLOUDY output models to work out our emission-line fluxes and EWs. In addition to varying the input stellar age, initial metallicity and inclusion of interacting binaries, we also vary the properties of the surrounding gas by varying the gas density and the ionization parameter.

To aid our interpretation of these CCSN host nebula regions, we use our nebular emission models from Xiao et al. (2018) to predict where stellar populations should lie in these BPT diagrams. Fig. 6 shows a selection of our models at ages of $\log(\text{age}) = 6.5$ and 7.0 yr^{-1} , with a hydrogen density of $\log(n_H) = 2 \text{ cm}^{-3}$ over a reasonable range of ionization parameters.

¹The models are available at: <http://bpass.auckland.ac.nz>.

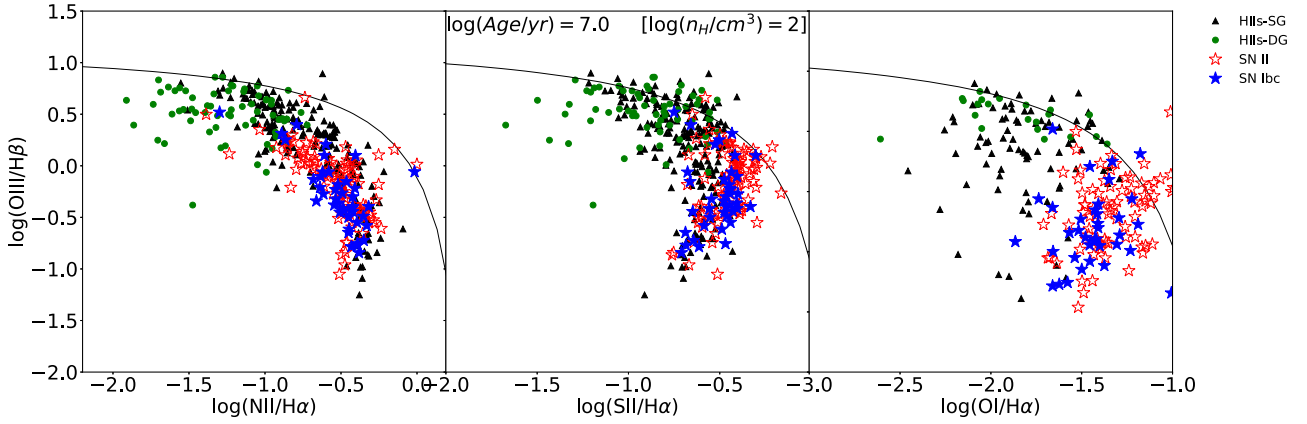


Figure 5. Distributions of H II regions of CCSN hosts in BPT diagrams compared to the van Zee sample of H II regions (the black triangles from spiral galaxies and green circles from dwarf galaxies). The SNe II hosts are represented by the red stars and SNe Ibc hosts are represented by the blue stars.

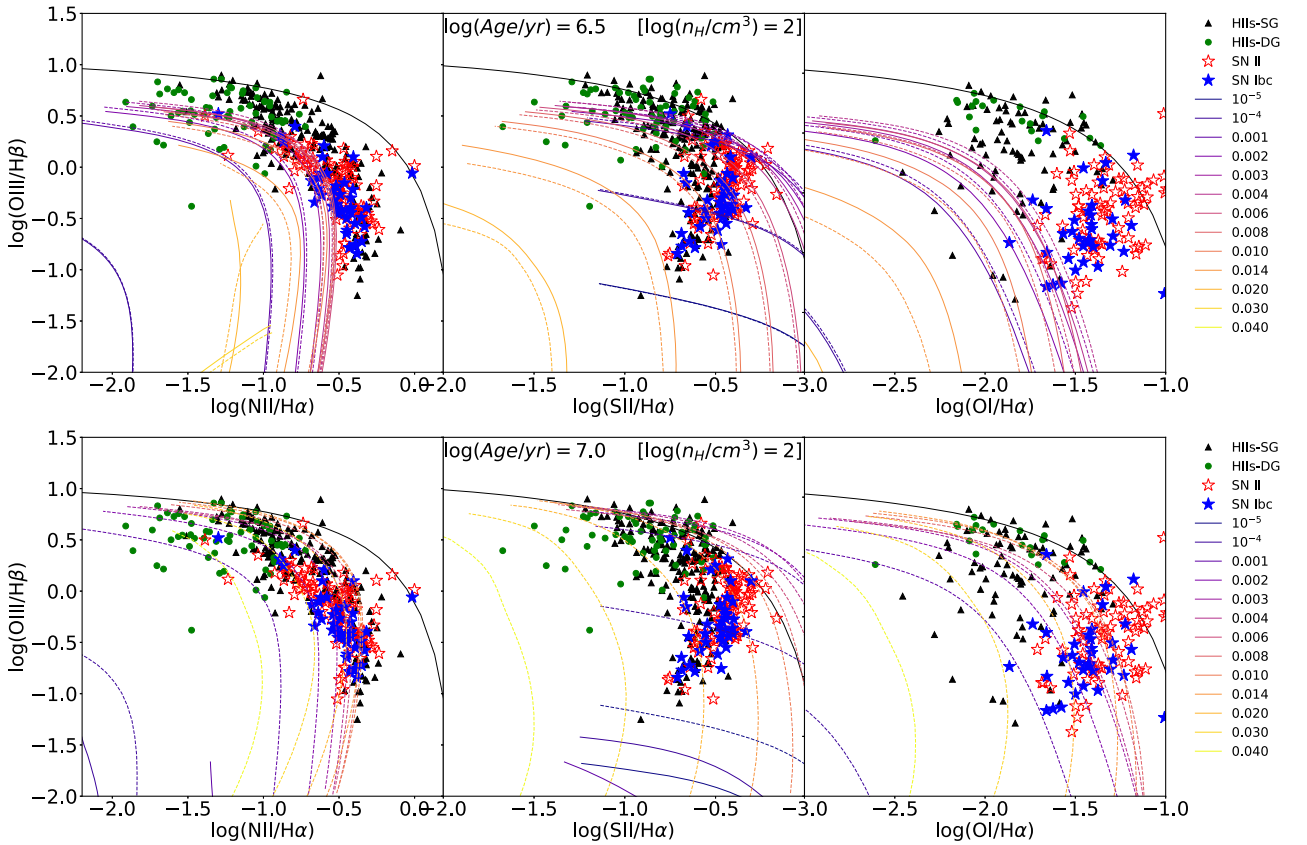


Figure 6. The BPT diagrams of BPASS models at 3 Myr (top panel) and 10 Myr (bottom panel). The tracks in solid lines are from single-star models and those in dashed lines are binary-star models. The tracks with different colours denote different metallicities from blue to red metallicity growing from $Z = 0.0001$ to 0.040. The value of the ionization parameter of the models is reduced following the track from upper left, $\log(U) = -1.5$, to lower right, $\log(U) = -4.5$.

As in Xiao et al. (2018), the nebular emission models of different metallicities produced 13 separated tracks. The models with lower metallicities ($Z < 0.020$) extend from upper left to lower right as the ionization parameter decreases from $\log(U) = -1.5$ to -4.5 . The three models with the highest metallicities ($Z = 0.020, 0.030$ and 0.040) have more vertical pathways that fall off with a decreasing ionization parameter. At 3 Myr, models with either too low or too high metallicity cannot match the observed CCSN hosts, and models of $Z = 0.001$ – 0.020 can only go through part of

the CCSN host area. However, as the population ages to 10 Myr, tracks from single-star models die away quickly. In contrast, those from binary-star models move up and match all the nebula regions. This result again highlights the importance of binary interactions in interpreting the emission lines from these CCSN hosts at later times.

With our full suite of models, we are able to perform a maximum likelihood fitting method to derive the preferred model parameters for each observed fitting region, rather than just comparing our

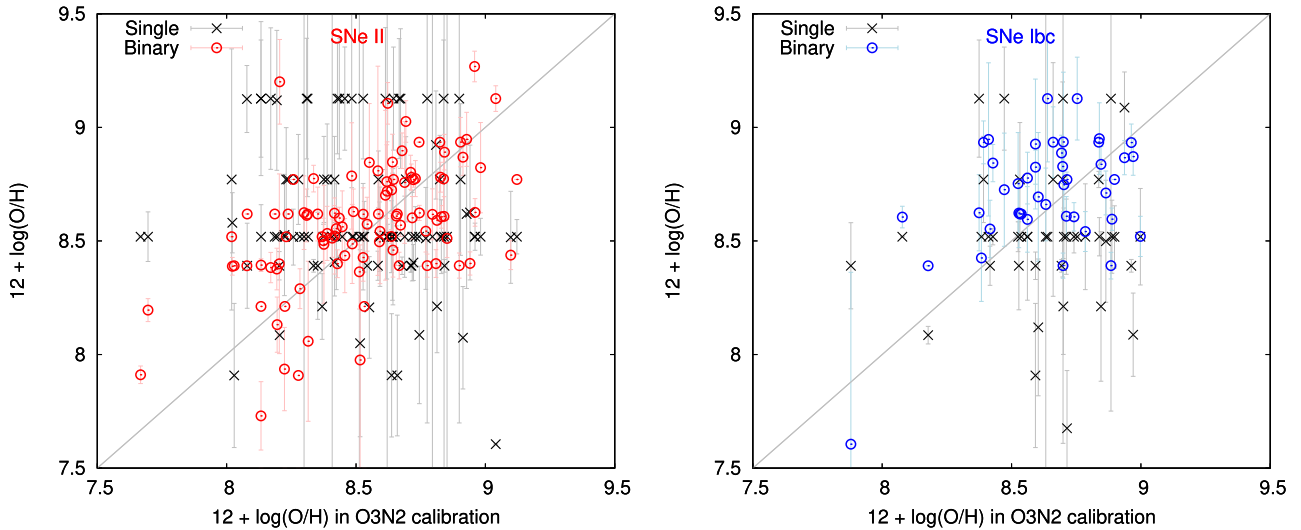


Figure 7. Predicted oxygen abundance from best-fitting models compared with those using O3N2 calibration. It shows the comparison between single- and binary-star models separately for SNe II and SNe Ibc hosts in the left and right panels, respectively. Single-star models are presented by the black crosses with error bars and binary-star models are denoted by the red (SNe II) and blue (SNe Ibc) circles with error bars.

models to the observed nebula regions by eye. For full details of the BPASS models, the nebular emission models and the fitting method, we refer the reader to Eldridge et al. (2017) and Xiao et al. (2018). Using these nebular emission-line models, we derived the properties of the underlying stellar population from the best-fitting models that match each individual H II region. The best-fitting parameters are listed in Tables A1 and A2. First, we use models that assume that none of the ionizing photons from the host stellar population is lost. Secondly, we allow for some leakage or loss of ionizing photons.

4 BEST-FITTING MODELS: NO LEAKAGE

4.1 Oxygen abundance measurement

Our best-fitting models are selected based on the emission-line ratios and our resultant oxygen abundance for each model is determined by the initial chemical composition for the model set, as described in Xiao et al. (2018). Here we can test the reliability of our best-fitting models by comparing the model abundances with those using O3N2 calibration, as shown in Fig. 7. In general, our binary-star models match the oxygen abundance in the O3N2 calibration better, although there is still considerable scatter around the line of equality. Single-star models show less variance in the distribution and have an oxygen abundance mostly of around 8.5. This result might suggest that our final fit for single-star populations is likely to be insensitive to the metallicity, compared with the results from our binary-star populations, and that their best fits are more dependent on other parameters of the emission nebula, which are discussed in detail in the following section. A lower metallicity model is probably preferable to match the observed emission-line ratios and to allow for hotter stars in the stellar population that are present in the binary populations. Given the correlation of our model input metallicity with the oxygen abundance in the O3N2 calibration as shown in Xiao et al. (2018), this calibration is a relatively good estimation of oxygen abundance for nearby H II regions with moderate metallicity. In particular, our models suggest significantly higher metallicity than that derived from O3N2 calibrations for the SNe II hosts with lower metallicities. Therefore, our models predict

similar oxygen abundance of the two SN types in a narrow range, which can indicate that the metallicity of the two SN types might not differ much in nearby galaxies.

4.2 Oxygen abundance variation with respect to U , n_H and age

While the oxygen abundances derived from our best-fitting models are important, the other input model parameters (i.e., the ionization parameter U , the gas density n_H cm⁻³ and the age of the inner ionizing stellar population source) tell us more about the surrounding environment of the SN and its stellar siblings. Table 2 provides an overview of the average of the best-fitting parameters. We note that the single and binary populations have similar average oxygen abundance and similar age, but there is a larger variance in oxygen abundance for binary-star models, as discussed previously, and there is larger variance in age for single populations. In addition, binary populations are distinguished from single populations by a lower ionization parameter and higher n_H .

Fig. 8 displays how oxygen abundances in our fits are related to these parameters for both SN types separately. We note that these SN nebular regions have a different $\log(U)$ distribution for our binary-star models compared with that expected for normal young H II regions, such as those in the van Zee sample that we have studied previously (Xiao et al. 2018). First, there is only a weak trend between oxygen abundance and $\log(U)$ distribution with most binary-star models concentrated between $\log(U) = -3.5$ and -3.0 , with higher values at lower metallicities. This suggests a significantly lower ionization state in these CCSN nebula regions than in young H II regions where $\log(U)$ up to -1.5 is more typical. These lower values are consistent with the position of the CCSN regions in the BPT diagrams, traced on the bottom region of the H II region sequence. For single-star models, they all have surprisingly high values of $\log(U)$ varying from -3 to -1 . For both model sets, there is little or no difference between the SN types.

Fig. 8 also shows the variation of oxygen abundance with respect to gas density $\log(n_H$ cm⁻³). For both SNe II and SNe Ibc, binary-star models vary over the full range of gas density. In contrast, most single-star models are concentrated at the highest hydrogen density

Table 2. The average value and standard deviation of oxygen abundance $12 + \log(\text{O}/\text{H})$, ionization parameter $\log(U)$, hydrogen density $\log(n_{\text{H}} \text{ cm}^{-3})$ and age, derived from best-fitting models.

No leakage	$12 + \log(\text{O}/\text{H})$	$\log(U)$	$\log(n_{\text{H}} \text{ cm}^{-3})$	$\log(\text{age yr}^{-1})$
Single	8.58 ± 0.20	-1.92 ± 0.69	2.91 ± 0.47	7.44 ± 0.51
Binary	8.60 ± 0.28	-3.36 ± 0.28	1.93 ± 0.94	7.56 ± 0.29

in our model of $\log(n_{\text{H}}) = 3.0 \text{ cm}^{-3}$. We find that this difference in density is closely correlated with ages of the inner ionizing source. Most typical H II regions are young with ages below 10 Myr, and the CCSN regions from the binary-star model fits mostly have ages beyond 10 Myr. This is consistent with their lower $\log(U)$ as less ionizing photon production occurs at later ages. In comparison, all the single-star model fits are at 10 Myr.

While the metallicity is determined primarily from the abundance of the gas being ionized, the other parameters are mostly determined by the ionization photon spectrum from the stellar population. Here, the difference between the single-star and binary-star models is because the interacting binaries allow hot stars to exist at ages beyond 10 Myr whereas there are no hot stars in the single-star models. Therefore, to achieve a fit, the single-star models have to resort to high gas densities and high ionization parameters to match the observed emission-line fluxes. The ages are then all around 10 Myr because this is the time when the EW of the lines decreases to match the observed values. Because the hardness of the ionizing spectra also drops, a very short-lived phase in the single-star models satisfies both ionizing spectrum and line strength constraints for the majority of the models. By contrast, the evolution is more gradual and there is a wider range of possible ages in the binary-star models. The values from the binary-star fits appear to be more sensible and realistic when compared with the estimated age of the stellar populations. Importantly, we detect no SNe that occur in a very young H II region hosting very massive young stars. There is a strong consensus here between single- and binary-star models that different types of SNe all arise from progenitors with ages beyond 10 Myr, equivalent to less massive progenitors with initial masses less than $20 M_{\odot}$.

5 EFFECT OF IONIZING PHOTON LEAKAGE

In the above analysis, we have assumed that every ionizing photon emitted from the stellar population contributes to the emission nebula flux. However, we know that in many regions some of these ionizing photons are lost, either by being absorbed and heating dust grains, or simply by escaping from the gas cloud before they have a chance to interact. In Xiao et al. (2018), we investigated the effect of ionizing photon leakage on reducing emission-line strength and how this altered the fit of models to H II regions. In general, we found that the best-fitting age with leakage included leads to generally younger H II regions, where the high EW values of the models meant they were otherwise disfavoured in the fitting calculation. In this section, we allow for this leakage or loss of ionizing photons to see if the derived ages change.

5.1 Oxygen abundance

First, the inclusion of ionizing photon leakage has a strong effect on the oxygen abundance measurement, as shown in Fig. 9. There are clear differences in the estimation of oxygen abundance compared with previous models without ionizing photon leakage. Both model sets now have a more linear relationship to the oxygen abundance

estimated from the O3N2 method. However, there is a significant offset between the single-star and binary-star models. The difference can be explained as follows. To achieve the same strength of the ionizing spectrum, single stars prefer lower metallicities where the average stellar temperatures are higher, whereas binary-star models have hotter post-main-sequence stars, even at higher metallicities, so they do achieve a reasonable fit without needing to decrease to a low metallicity. As a consequence, allowing leakage makes the metallicity predictions from the O3N2 method consistent with single-star models, because varying metallicity is the primary way to vary the hardness of the ionizing radiation from single stars. For the binaries, metallicity is a small effect because, for helium stars produced at late ages, the ionizing radiation hardness varies less. Nevertheless, we see no clear distinction between the range of host metallicity in the two CCSN types. Therefore, we can suggest that the similar ionizing photon leakage effect for these two CCSN hosts is probably a result of a similar ISM distribution within their host H II regions.

By comparing the average oxygen abundance and other physical parameters of the best-fitting models listed in Tables 2 and 3, we can again emphasize that the inclusion of ionizing photon leakage can change these best-fitting parameters significantly. Binary-star models increase their average oxygen abundance by nearly 0.2 dex, while single-star models decrease by about 0.1 dex, on average. For single-star models, this change in oxygen abundance is combined with $\log(U)$ being a factor of 2 lower and with age significantly decreasing by 1.2 dex, while there is little difference in hydrogen density $\log(n_{\text{H}} \text{ cm}^{-3})$. The binary-star models also experience a corresponding decrease in age by 0.5 dex, but have almost no change in $\log(U)$ and a slight decrease in $\log(n_{\text{H}} \text{ cm}^{-3})$. Therefore, we suggest that the most important effects of ionizing photon leakage are the reduction of age and the corresponding variance in oxygen abundance.

5.2 Variation of oxygen abundance with respect to U , n_{H} and age

When we consider the other model parameters that we obtain from our fit, we find that the inclusion of ionizing photon leakage leads to very different results. Again, the distributions of these two CCSN types are very similar but show differences compared with the previous result, as shown in Fig. 10. Now single-star models have shifted to lower ionization parameters, with $\log(U)$ between -4 and -3 , just as for the binary-star models. In addition, we find that the best-fitting models including ionizing photon leakage are more likely to show lower gas densities compared with previous models, although a significant fraction of the binary-star models still show high density with $\log(n_{\text{H}} \text{ cm}^{-3}) = 3$. The most significant difference is that the single-star models become much younger, with ages all below 3 Myr except for a few outliers. This also occurs for the binary-star models but more moderately so; most of the ages are between 10 and 30 Myr. All the single-star models are too young to be a reasonable age estimate of the SN progenitors. Even the most massive stars have a minimum evolution lifetime of the order of 3 Myr.

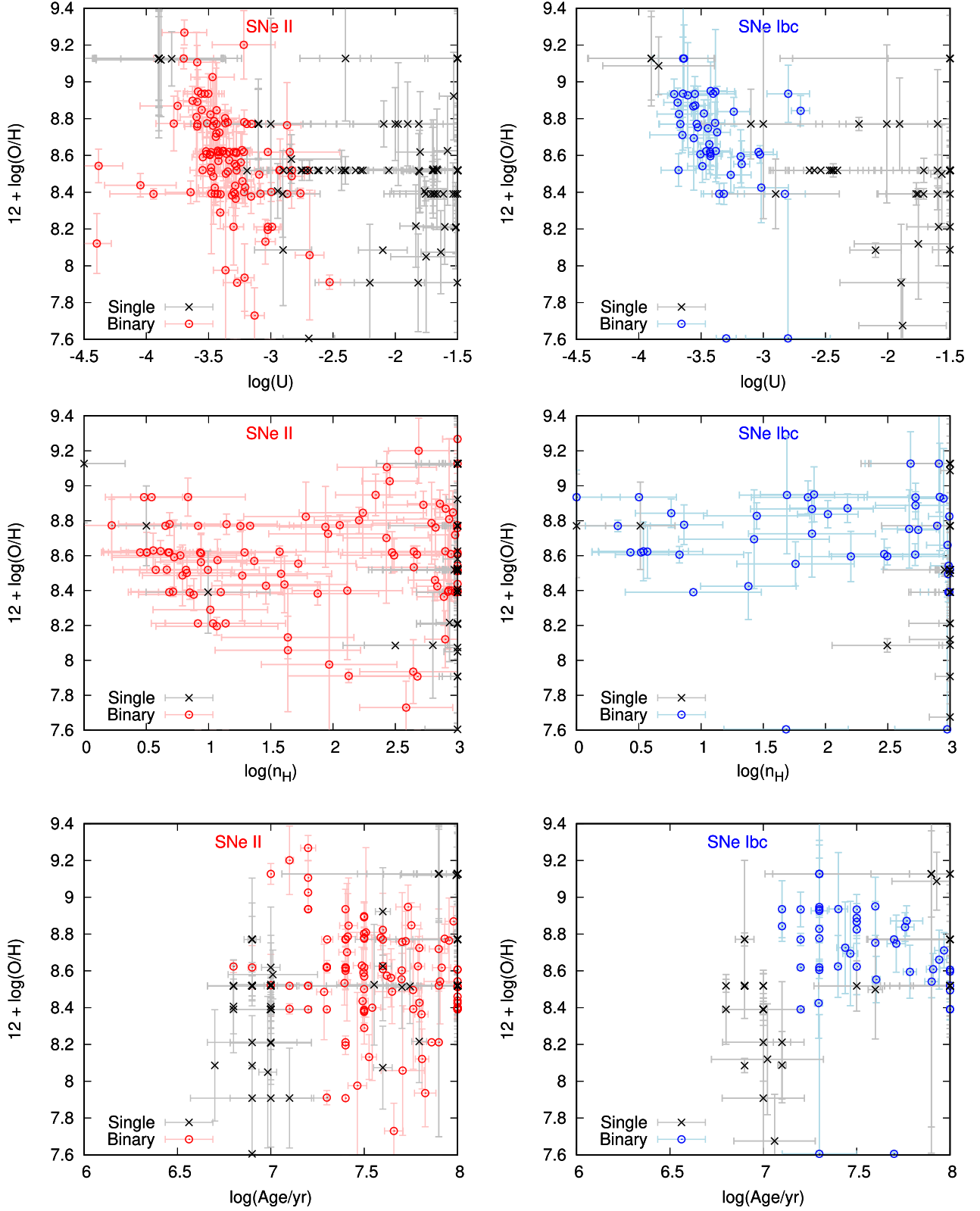


Figure 8. The variation of oxygen abundance with respect to ionization parameter $\log(U)$ for the SN hosts in the top panels, $\log(n_{\text{H}} \text{ cm}^{-3})$ in the middle panels and $\log(\text{age yr}^{-1})$ in the bottom panels, with the left panels for SNe II hosts and the right panels for SNe Ibc hosts. Single-star models are denoted by black crosses with error bars and binary-star models by red (SNe II) and blue (SNe Ibc) crosses with error bars.

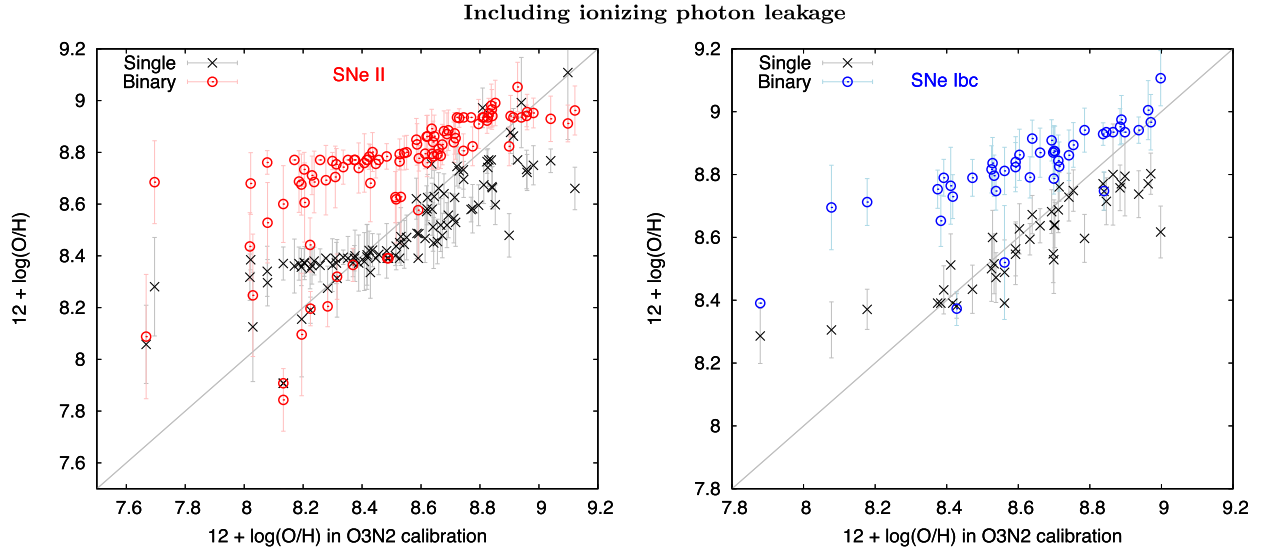


Figure 9. Predicted oxygen abundance from best-fitting models with ionizing photon leakage, compared with those using O3N2 calibration. The figure shows a comparison between single-star and binary-star models separately for SNe II hosts (left panel) and SNe Ibc hosts (right panel). Single-star models are presented by the black crosses with error bars and binary m-star models are the red (SNe II) and blue (SNe Ibc) crosses with error bars.

Table 3. Including ionizing photon leakage, the average value and standard deviation of oxygen abundance $12 + \log(\text{O}/\text{H})$, ionization parameter $\log(U)$, hydrogen density $\log(n_{\text{H}} \text{ cm}^{-3})$ and age, derived from best-fitting models.

Leakage	$12 + \log(\text{O}/\text{H})$	$\log(U)$	$\log(n_{\text{H}} \text{ cm}^{-3})$	$\log(\text{age yr}^{-1})$
Single	8.46 ± 0.32	-3.27 ± 0.40	2.48 ± 0.53	6.22 ± 0.33
Binary	8.75 ± 0.24	-3.36 ± 0.38	1.48 ± 0.61	7.09 ± 0.59

The age and metallicity ranges of the binary-star models are shown more clearly in Fig. 11. These agree with similar observational constraints from detected SN progenitor detections (Smartt 2015) and from resolved stellar populations (Williams et al. 2018). These ages imply initial masses for most of the SNe in our sample of approximately $8\text{--}20 M_{\odot}$. This is approximately the mass above which it is expected that core collapse produces black holes that might not lead to visible SNe (e.g. Heger et al. 2003; Eldridge & Tout 2004; Zapartas et al. 2017). As the $\text{H}\alpha$ EW is a sensitive tracer of age at higher metallicities ($Z > 0.004$), as shown in Fig. 3, the similar age distributions of the two SN types are incorporated with their almost identical distributions of $\text{H}\alpha$ EWs, as shown in Fig. 2. In addition, we note that while the bulk of SNe of both types are seen across a similar range of metallicities, the fraction of events does appear to change with metallicity. At metallicities below $12 + \log(\text{O}/\text{H}) \sim 8.5$, the number of Type Ibc events drops off sharply, while SNe II drop off less rapidly and so become relatively more common.

5.3 Extent of remaining ionizing photons

Given that a large fraction of ionizing photons must escape to provide the best fits to the data, it is interesting to consider the fraction of remaining ionizing photons, which are absorbed and processed by the nebular gas. Xiao et al. (2018) discussed the remaining ionizing photon fraction as a function of age in H II regions in nearby dwarf and spiral galaxies. Here, Figs 12 and 13 present the fraction of photons remaining to interact with the nebular gas after accounting for photon leakage, f_{rem} , as a function of age and EW respectively for CCSN host regions. Compared to the equivalent fraction in Xiao

et al. (2018), the CCSN hosts experience more ionizing photon leakage, with roughly an order of magnitude lower f_{rem} for single-star models, while in the binary-star model fits, the typical remaining fractions are a factor of 2 lower than in our previous study. This is a corollary of the young ages required in the single-star model fits: the observed data require a very high photon production rate to explain the ionization state but must then lose most of the photons in order to explain the recombination-line EW. For binary stars, already a more efficient source of hard ionizing photons, a smaller escape fraction is required. The 50 per cent ionizing photon leakage typically required by binary-star models is consistent with the fact that CCSN hosts are relatively old and more defused nebulae, through which ionizing photons might have a sufficiently long mean free path to escape without interaction.

6 DISCUSSION

In this paper, we have attempted to constrain the age and metallicity of nearby SN progenitors by modelling the nebular emission lines from the stellar populations surrounding the SN site. Using single-star stellar populations, we have found that emission-line ratios imply a combination of unrealistically dense gas, young stellar populations and high ionization parameters. In comparison, models that take account of interacting binary stars provide much better and more realistic parameters for the SN progenitors. The estimated model parameters have lower gas densities, lower ionization parameters and older ages, which would be expected for stellar populations where the bulk of SNe should occur. The nebular regions hosting CCSNe must already have lost their most massive stars, which collapse to black holes and are unlikely to form optically

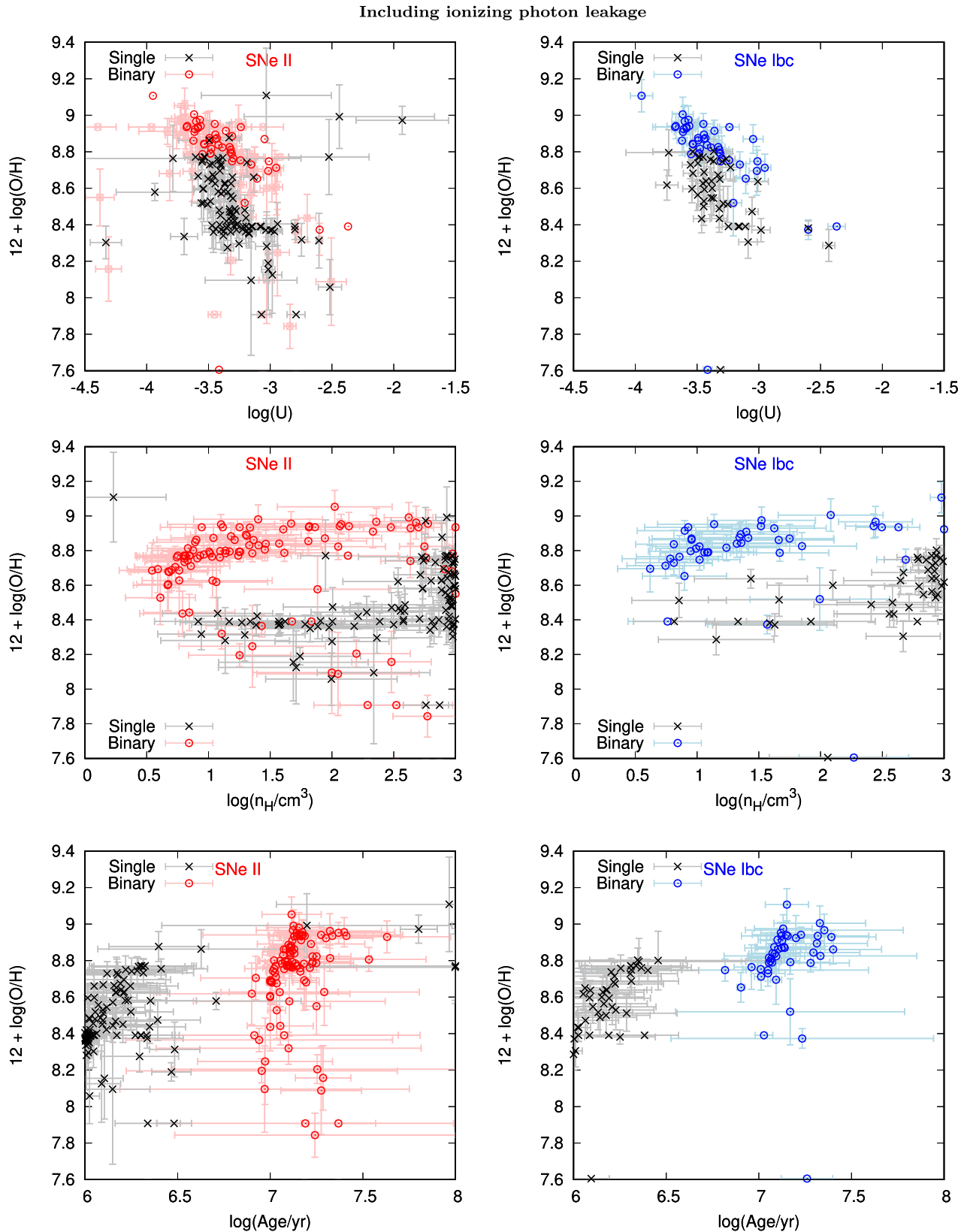


Figure 10. The variation of oxygen abundance in the ionizing photon leakage case with respect to the ionization parameter $\log(U)$ for the SN hosts (top panels), $\log(n_{\text{H}} \text{ cm}^{-3})$ (middle panels) and $\log(\text{age yr}^{-1})$ (bottom panels), with the left panels for SNe II hosts and the right panels for SNe Ibc hosts. Single-star models are denoted by black crosses with error bars and binary-star models by red (SNe II) and blue (SNe Ibc) circles with error bars.

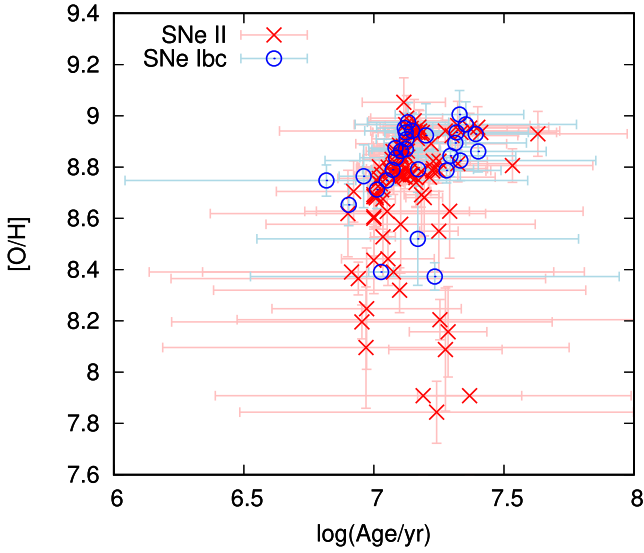


Figure 11. Age constraints on SNe II and SNe Ibc progenitors from binary-star models. Red crosses with error bars are for SNe II and blue circles with error bars are for SNe Ibc.

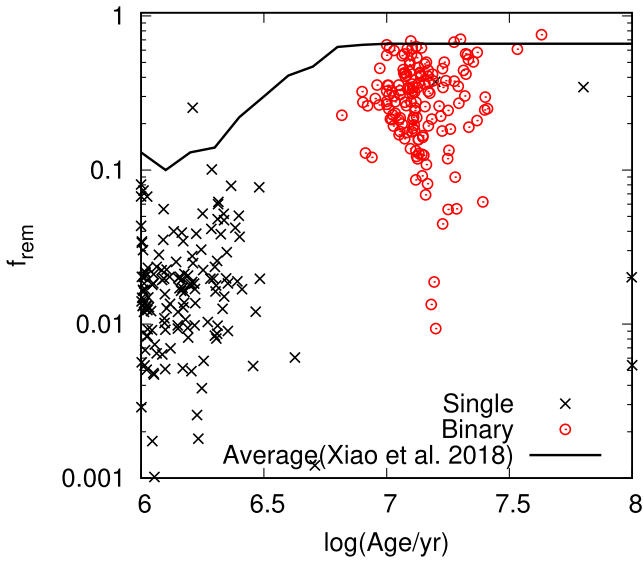


Figure 12. The fraction of remained ionizing photon leakage, f_{rem} , as a function of age. The black crosses are for single-star models and the red circles are for binary-star models. For comparison, the solid line indicates the fractions inferred using an identical analysis for a large sample of typical H II regions in spiral and dwarf galaxies by Xiao et al. (2018).

luminous transients, or alternatively evolve into ultraluminous and very rare transients. Instead, they must be old enough to reach the terminal age of less massive stars that die as normal SNe. Thus, they should differ from the very young, often ultraviolet- or H α -selected, star-forming regions, which are dominated by the most massive stars and are more conventionally identified by H II region surveys. These regions have high ionization parameters and gas densities (e.g. Xiao et al. 2018) and so the fact that our binary-star model fits are not like this is consistent with what we should expect.

An important question is to decide whether we should favour our derived parameters assuming leakage or no leakage. To answer this question, first we consider Figs 14, 15 and 16 that compare the pre-

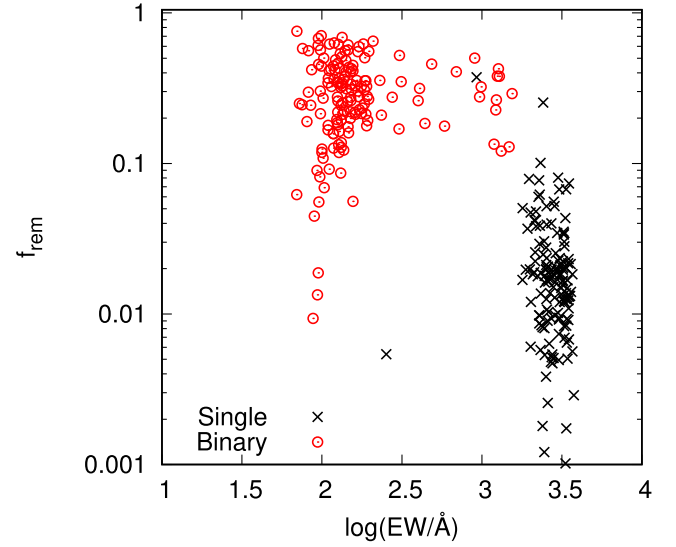


Figure 13. The fraction of remained ionizing photon leakage, f_{rem} , as a function of EW. The black crosses are for single-star models and the red circles are for binary-star models.

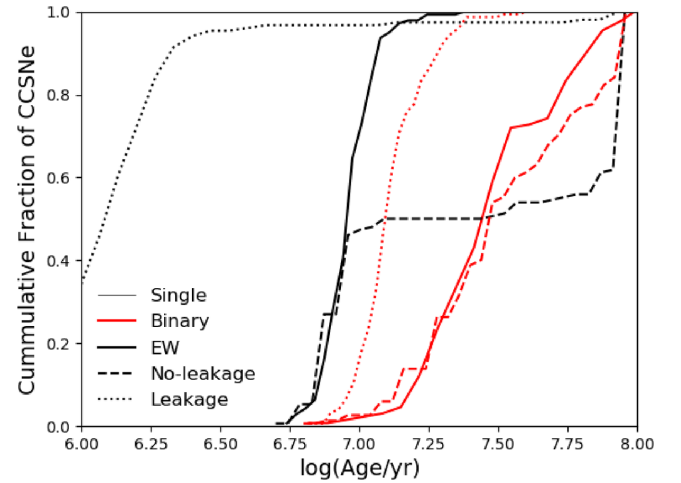


Figure 14. Cumulative fraction of CCSNe as a function of age derived using the three methods: directly from the H α EW (solid lines), best-fitting models without ionizing photon leakage (dashed lines) and best-fitting models including leakage (dotted lines). The single-star models are denoted by black lines and binary-star models by red lines.

dicted age of the SNe from the three methods to determine the age, H α EW and emission-line fitting without and with ionizing photon leakage. We see that the H α EW age and no-leakage emission-line fits agree closely. This reflects the fact that the H α EW drives the age in our fitting algorithm, while the line ratios are more sensitive to alternative parameters. However, allowing for leakage decreases the ages derived from the emission-line fits. For the single-star models, these ages are unrealistically young at 3 Myr and below, whereas for binary-star models, the change does allow the ages to be more plausible, with most lying between 10 and 30 Myr.

Theoretical predictions for the age distribution of SNe in both Zapartas et al. (2017) and Eldridge et al. (2017) show that the SN rate in binary-star models is highest at younger ages and decreases at older ages. This is because even though there are more lower-mass stars, their evolutionary time-scale becomes more dependent

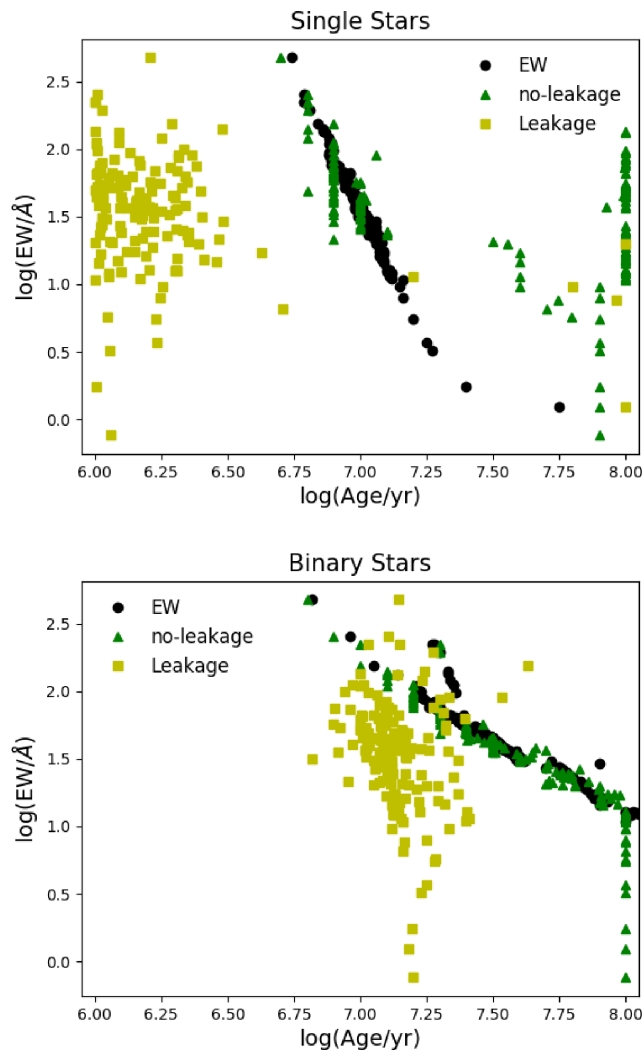


Figure 15. The $H\alpha$ EW versus derived age from the EW-based method and best-fitting models with and without ionizing photon leakage. The black dots represent the EW-based ages and the green triangles and yellow squares are ages from no-leakage and leakage best-fitting models, respectively.

on mass and so they are spread out over a larger time. We see that for our preferred binary-star models assuming leakage, although there are some SNe with ages as young as 6 Myr, the majority have ages of 10 Myr and above. This agrees with the initial mass range at which there is a change in remnant formation from neutron stars to black holes, at round $20 M_{\odot}$ (Eldridge & Tout 2004), although we note that the situation might not be as simple as there being one single cut-off mass (e.g. Sukhbold & Woosley 2014; Ertl et al. 2016). In the no-leakage case, the majority of our derived SN ages are beyond 30 Myr and up to 100 Myr when these should be the rarest events. Therefore, this suggests that our derived ages with leakage are a more accurate age estimate for the SN progenitor. This leakage fraction will also incorporate a factor of dilution of the emission lines from any underlying old stellar population that might also be contributing to the continuum flux. Nevertheless, recent studies of SNe and supernova remnants (SNRs) suggest that SN progenitors would tend to be from older populations. For example, Zapartas et al. (2017) predict that about 15 per cent of CCSNe originating from binary-star systems are late to occur 50–200 Myr after birth. Then recently, Díaz-Rodríguez et al. (2018) have analysed the stellar

population surrounding 94 SNRs in M31 and M33, where they found some SNRs to have associated stellar populations older than 30 Myr, up to 80 Myr. Thus, our findings add to the growing evidence that some CCSNe arise from older stellar populations.

An important deduction we can make from Figs 14 and 16 is that the use of the single-star $H\alpha$ EW provides a reasonable age estimate for SN progenitors. The difference in the single-star EW ages and the binary-star models with leakage is only approximately 0.2 dex. Thus, one simple conclusion we could make is that all SN progenitor ages derived by $H\alpha$ underestimate the stellar population ages by approximately 60 per cent, and thus overestimate the initial progenitor mass (e.g. Chen et al. 2017). In Fig. 15, we show that it is possible to use our work to calibrate a crude but broadly correct $H\alpha$ EW to the age relation. However, this relation shows a large scatter because of the range of metallicities and gas conditions in the sample and we highly recommend that the age should be derived using a full set of nebular emission lines to provide greater accuracy.

It is also worthwhile to compare our age ranges to other estimates from progenitor and stellar population studies that are extant in the literature. We show the results of such a test in Table 4, where we include the SNe for which pre-explosion images exist that enable constraints to be placed on the initial masses of the progenitor stars. We have used the masses from Eldridge et al. (2013) and Smartt (2015), converting the masses to estimated progenitor lifetimes using our stellar models. We also list the lower age limit from the progenitor detection and we include age estimates by Maund & Ramirez-Ruiz (2016) and Maund (2017, 2018) who have used similar imaging to study the stellar populations surrounding SN sites. From this, they derive the ages of the largest stellar populations, which we list here. However, we note that the ages were derived using single-star evolution tracks and we ignore the effect of interacting binaries on the stellar population. Therefore, these ages are likely to be underestimates (Eldridge et al. 2017).

We see that most of the progenitor ages lie in the region of around $\log(\text{age}) = 6.8\text{--}7.7 \text{ yr}^{-1}$. While the uncertainties are large, there is consistency between these ages and those from our binary population ages. In most cases, our single-star estimates give values that are either too old or too young. However, it is difficult to decide whether we should include our leakage model or not. In general, the no leakage binary-star model tends to provide a fit with low uncertainty that can be significantly old when the SN rate is expected to be low. With leakage, the ages are younger, although with a higher uncertainty in some cases. We find that this still suggests that our inclusion of leakage provides a more reasonable fit. We note there is other secondary evidence for SN 2007gr. Mazzali et al. (2010) studied the light curve of 2007gr and found that the SN is consistent with the explosion of a $15 M_{\odot}$ star. This is consistent with a lifetime of $\log(\text{age}) = 7.1 \text{ yr}^{-1}$, which is consistent with our ages but not that of Maund & Ramirez-Ruiz (2016). The reason for this mismatch is likely to be because their age derivation was made using single-star evolution tracks. If a fit were carried out with a binary population (e.g. as for Cygnus OB in Eldridge et al. 2017), then the age would likely become consistent with the older age.

A final view on our results is the relationship between metallicity and progenitor age. We see in Fig. 11 that, in general, the two different types of SNe cover similar ranges of ages and oxygen abundance values but the oldest progenitors as well as the lowest metallicity events are for SNe II. This is in agreement with predictions by authors such as Heger et al. (2003) and Eldridge & Tout (2004), because these stars experience less mass loss over their lives. The older, less-massive stars have weaker winds while, at

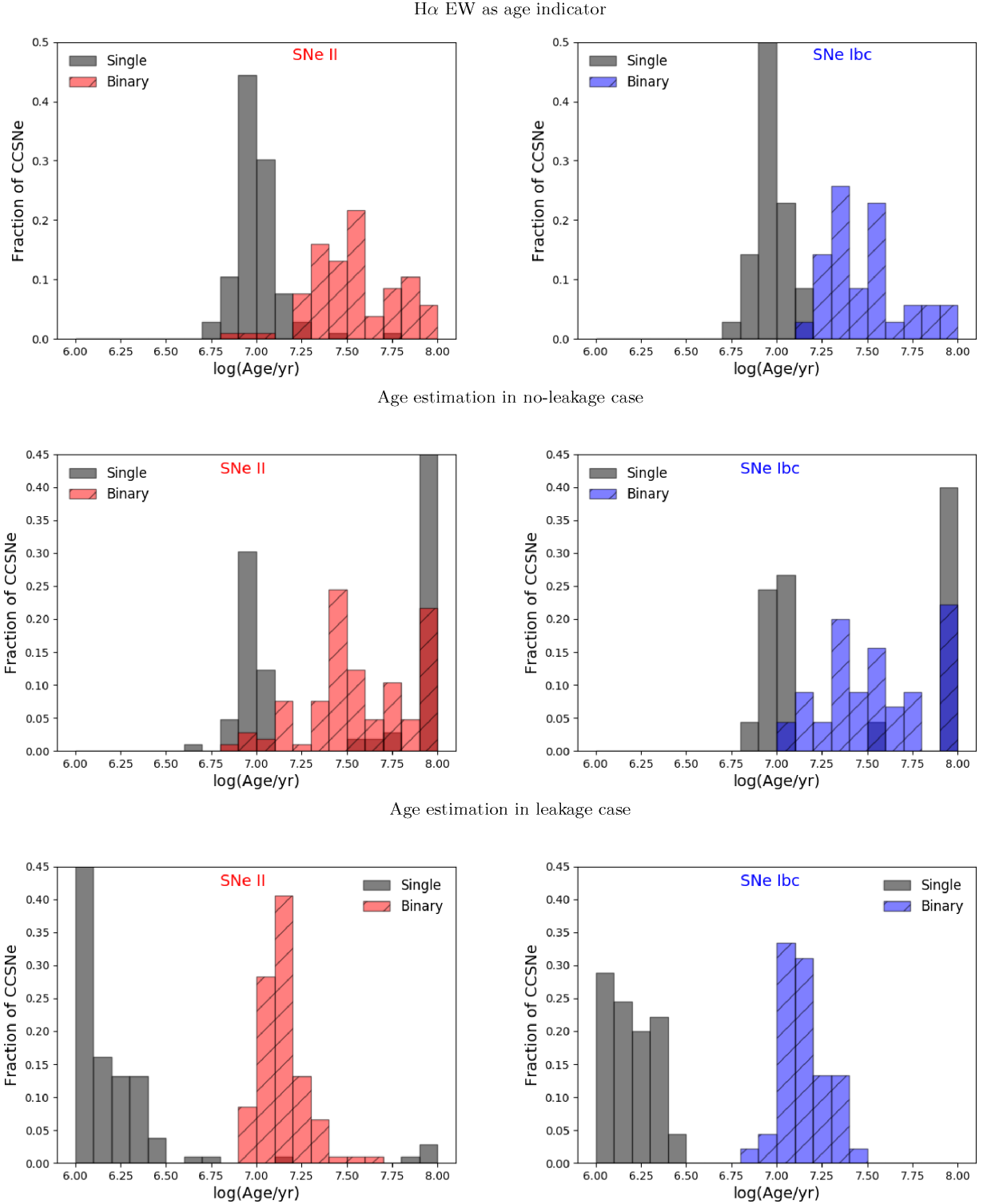


Figure 16. The fraction of CCSNe as a function of age derived using the three methods: directly from the H α EW (top panels), best-fitting models without ionizing photon leakage (middle panels) and best-fitting models including leakage (bottom panels). The left panels show the fraction distribution for SNe II and the right panels for SNe Ibc. The black bars are for single-star models and red (SNe II) and blue (SNe Ibc) bars are for binary-star models.

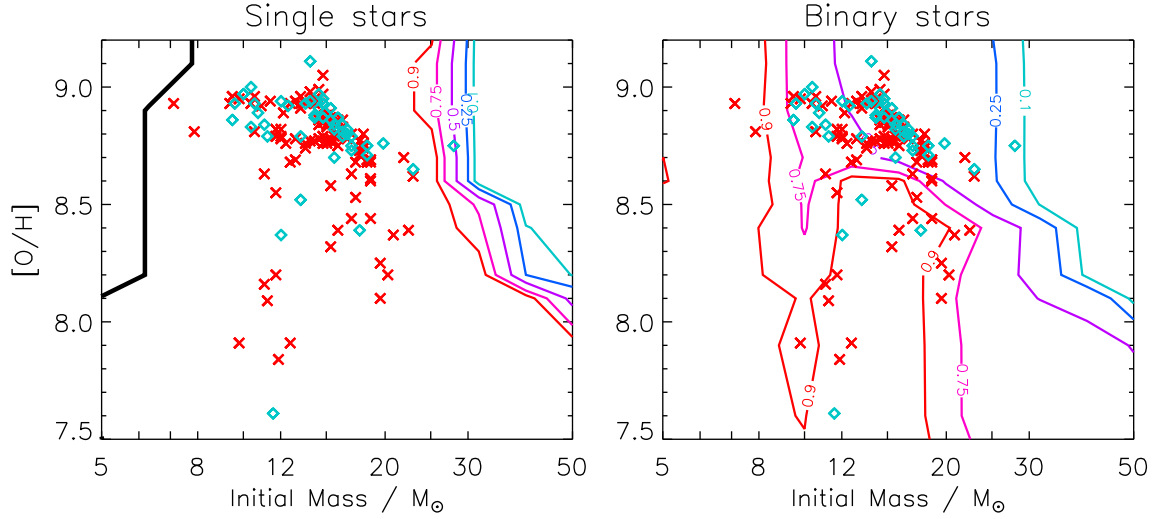
lower metallicities, line-driven winds are weaker for stars of the same metallicity.

Another way to see how our derived ages and metallicities from the emission lines compare with model SN predictions is to convert our ages into effective initial masses. We use our single-star models

to determine a relation between the age of a stellar population and the mass of a single star with the same lifetime. Using these values we have created Fig. 17, which is similar to the widely used figure in Heger et al. (2003), which shows the regions where different SN types occur in initial mass versus initial metallicity

Table 4. Comparison of ages derived by our method with those for SNe with progenitor detections or constraints (Smartt 2015; Eldridge et al. 2013) and surrounding stellar population constraints (Maund & Ramirez-Ruiz 2016; Maund 2017, 2018).

SN name	SN type	Progenitor		Maund stellar populations log (age yr ⁻¹)	No leakage		Leakage	
		Best estimate log (age yr ⁻¹)	Lower limit log (age yr ⁻¹)		Single log (age yr ⁻¹)	Binary log (age yr ⁻¹)	Single log (age yr ⁻¹)	Binary log (age yr ⁻¹)
2003gd	IIP	7.7	>7.3	7.14, 8.08	6.9 ± 0.0	7.49 ± 0.05	6.30 ± 0.19	7.08 ± 0.73
2013ej	IIP	7.4	>7.2	7.16, 8.03	8.0 ± 0.38	7.93 ± 0.12	6.12 ± 0.26	7.13 ± 0.07
1999gi	IIP	–	>7.2	–	6.9 ± 0.04	7.4 ± 0.0	6.40 ± 0.27	7.18 ± 0.54
1999em	IIP	–	>7.1	–	8.0 ± 0.78	8.0 ± 0.0	6.10 ± 0.24	7.12 ± 0.02
2007gr	Ic	6.8 or 7.3	>6.8	6.79, 7.69	8.0 ± 0.7	7.94 ± 0.04	6.19 ± 0.22	7.17 ± 0.21
2001B	Ib	–	–	6.55, 7.14	7.0 ± 0.22	7.3 ± 0.04	6.21 ± 0.24	7.09 ± 0.15

**Figure 17.** The predicted number count ratio of SN type as a function of initial mass and metallicity, compared with observational data (SNe II, red crosses; SNe Ibc, blue diamonds) from the best-fitting models accounting for ionizing photon loss. The contours are annotated with the fraction of SNe II at that contour. The thick black line represents the minimum initial mass for SNe to occur.

space. These figures show similar structures to our earlier attempts at these figures in Eldridge & Tout (2004). Here, however, we use oxygen abundance rather than the metallicity mass fraction to measure the metal enrichment. The first panel, which shows where different SN types occur for single stars, demonstrates that for the initial masses and metallicities we derive, all SNe in our sample should be Type II. Therefore, most SN progenitors cannot arise from single-star progenitors.

The problem with creating a binary version of these progenitor figures is that there is no longer a direct connection between initial mass and final evolutionary outcome. This is because of the many diverse possible evolutionary pathways that become possible due to binary interactions. Our attempt at such a figure is shown in the second panel of Fig. 17. It was created by looking at all stars from our binary-star models that have the same initial mass and initial metallicity. We use logarithmic mass bins of 0.1 dex width and we use metallicity bins for our source models. Then, for each model that lies in a specific bin that experiences a CCSN (if the final mass is $>1.5 M_{\odot}$, the CO core mass is $>1.38 M_{\odot}$ and core carbon burning has occurred), we identify if they are SNe II or SNe Ibc by the hydrogen mass in the model (if it is $>10^{-3} M_{\odot}$, then the SN is Type II). From this, at each point in the progenitor figure, we can work out the fraction of SNe that are Type II, with the remainder being Type Ibc. We then draw contours of these values of the initial parameter space, and the resulting figure shows for

which initial parameters SNe II and SNe Ibc are most common. We see that at high masses and metallicities most of the SNe are Type Ibc due to stellar wind mass loss. At lower masses, especially at lower metallicities, most SNe are Type II because even though binary interactions might remove a significant amount of surface hydrogen, the stellar winds are unable to remove the remaining hydrogen before core collapse.

The location of the SN progenitor masses and metallicities we derive here broadly agrees with these models. A mix of events occurs close to the even mix of SN types while more SNe II occur relative to SNe Ibc where this is predicted. It is important to note that the same models that went into the creation of the contours in this figure are also those that are used to evaluate and characterize the stellar population at the location of the SNe, and hence to estimate the progenitors. However, different aspects of those models were used. For example, we used the amount of hydrogen remaining at the end of the progenitors' lives to estimate their type, while for the emission-line fitting we used the total luminous output of the stellar models at the same age. Therefore, a key result from this figure is that the average SN type we infer from the surrounding emission-line output of a living stellar population is related to the most likely SN type (i.e. if there are a number of stars that have lost their hydrogen envelopes to form helium stars, then the emission lines will reflect this and it will be more likely that a SN Ibc will occur). In contrast, fewer stars will have lost their hydrogen envelope, so

fewer hot helium stars contribute to the stellar population, and SNe II become more common than SNe Ibc.

These helium stars are a common prediction of stellar models that include binary interactions. Although they have not yet been observed in our own Galaxy, we can be sure from their impact, in the ionizing photon production in galaxies (Stanway, Eldridge & Becker 2016; Götberg et al. 2017) and in creating SNe Ibc, that they must exist (Eldridge et al. 2013; Eldridge & Maund 2016). These stars, while currently ‘invisible’ nearby in our Galaxy, have important impacts on more distant stellar populations. Ignoring these can lead to inconsistencies and errors in studies of stellar systems, especially in young populations where the binary fraction is high.

7 CONCLUSIONS

Our main conclusions of this work are as follows.

(i) To accurately understand the emission-line nebulae at SN sites, we must account for interacting binaries in the stellar populations and allow for some loss of ionizing photons.

(ii) When we derive our best-fitting ages for SN progenitors, assuming binary stellar populations we find that both SNe II and SNe Ibc progenitors typically have ages of 10–30 Myr, and therefore they are less-massive stars with initial masses $M \leq 20 M_{\odot}$.

(iii) We find no single, monotonic relation between metallicity, initial mass and eventual SN type as predicted for single stars in Heger et al. (2003). Instead, binary interactions must be taken into account and we find that the expected mean SN type is related to the emission nebula created by the stellar population surrounding the SN site. This is shown by the fact that the binary-star models provide a much improved prediction of the Type II to Ibc ratio as a function of progenitor mass and metallicity than single-star models.

(iv) It is possible to derive an approximate relation between the age of a SN progenitor and the $H\alpha$ EW, although a more accurate age can be derived by using all available emission lines.

These findings indicate that when modelling the nebular emission from stellar populations interacting binaries must be included. Use of the techniques we outline here will provide a new rigorous method to understand CCSNe.

ACKNOWLEDGEMENTS

LX acknowledges grants from the National Key R&D Programme of China (2016YFA0400702), the National Natural Science Foundation of China (Nos 11673020 and 11421303) and the National Thousand Young Talents Programme of China. LX would also like to thank the China Scholarship Council for its funding of her PhD study at the University of Auckland and the travel funding and support from the University of Auckland. LG was supported in part by the US National Science Foundation under Grant AST-1311862. JJE acknowledges travel funding and support from the University of Auckland. The authors also wish to acknowledge the contribution of the NeSI high-performance computing facilities and the staff at the Centre for eResearch at the University of Auckland. New Zealand’s national facilities are provided by the New Zealand eScience Infrastructure (NeSI; <http://www.nesi.org.nz>) and funded jointly by NeSI’s collaborator institutions and through the Ministry of Business, Innovation and Employment’s Infrastructure programme. We also thank the reviewer and the editor for the thoughtful and helpful comments that greatly improved the paper.

REFERENCES

- Anderson J. P., James P. A., 2008, *MNRAS*, 390, 1527
 Baldwin A., Phillips M. M., Terlevich R., 1981, *PASP*, 93, 817
 Chen T.-W. et al., 2017, *ApJ*, 849, L4
 Crowther P. A., 2013, *MNRAS*, 428, 1927
 De Donder E., Vanbeveren D., 1997, *A&A*, 318, 812
 De Donder E., Vanbeveren D., 1998, *A&A*, 333, 557
 de Wit W. J., Testi L., Palla F., Zinnecker H., 2005, *A&A*, 437, 247
 Díaz-Rodríguez M., Murphy J. W., Rubin D. A., Dolphin A. E., Williams B. F., Dalcanton J. J., 2018, *ApJ*, 861, 92
 Eldridge J. J., Fraser M., Smartt S. J., Maund J. R., Crockett R. M., 2013, *MNRAS*, 436, 774
 Eldridge J. J., Izzard R. G., Tout C. A., 2008, *MNRAS*, 384, 1109
 Eldridge J. J., Langer N., Tout C. A., 2011, *MNRAS*, 414, 3501
 Eldridge J. J., Maund J. R., 2016, *MNRAS*, 461, L117
 Eldridge J. J., Stanway E. R., Xiao L., McClelland L. A. S., Taylor G., Ng M., Greis S. M. L., Bray J. C., 2017, *PASA*, 34, e058
 Eldridge J. J., Tout C. A., 2004, *MNRAS*, 353, 87
 Ertl T., Janka H.-Th., Woosley S. E., Sukhbold T., Ugliano M., 2016, *ApJ*, 818, 124
 Ferland G. J., Korista K. T., Verner D. A., Ferguson J. W., Kingdon J. B., Verner E. M., 1998, *PASP*, 110, 761
 Ferland G. J. et al., 2013, *Rev. Mex. Astron. Astrofis.*, 49, 137
 Galbany L. et al., 2014, *A&A*, 572, A38
 Galbany L. et al., 2016a, *MNRAS*, 455, 4087
 Galbany L. et al., 2016b, *A&A*, 591, A48
 Galbany L. et al., 2018, *ApJ*, 855, 107
 Gonzalez Delgado R. M., Perez E., 1997, *Rev. Mex. Astron. Astrofis. Conf. Ser.*, 6, 264
 Graur O., Bianco F. B., Huang S., Modjaz M., Shivvers I., Filippenko A. V., Li W., Eldridge J. J., 2017, *ApJ*, 837, 120
 Götberg Y., de Mink S. E., Groh J. H., 2017, *A&A*, 608, 11
 Hakobyan A. A. et al., 2017, *MNRAS*, 471, 1390
 Heger A., Fryer C. L., Woosley S. E., Langer N., Hartmann D. H., 2003, *ApJ*, 591, 288
 Kewley L. J., Dopita M. A., Sutherland R. S., Heisler C. A., Trevena J., 2001, *ApJ*, 556, 121
 Kewley L. J., Ellison S. L., 2008, *ApJ*, 681, 1183
 Kissler-Patig M., Copin Y., Ferruit P., Pécontal-Rousset A., Roth M. M., 2004, *Astron. Nachr.*, 325, 159
 Kuncarayakti H. et al., 2013a, *AJ*, 146, 30
 Kuncarayakti H. et al., 2013b, *AJ*, 146, 31
 Kuncarayakti H. et al., 2017, *A&A*, 613, A35
 Lopez L. A., Krumholz M. R., Bolatto A. D., Prochaska J. X., Ramirez-Ruiz E., 2011, *ApJ*, 731, 91
 Maeder A., Meynet G., 2004, *A&A*, 422, 225
 Marino R. A. et al., 2013, *A&A*, 559, A114
 Mast D. et al., 2014, *A&A*, 561, A129
 Maund J. R., 2017, *MNRAS*, 469, 2202
 Maund J. R., 2018, *MNRAS*, 476, 2629
 Maund J. R., Ramirez-Ruiz E., 2016, *MNRAS*, 456, 3175
 Mazzali P. A., Maurer I., Valenti S., Kotak R., Hunter D., 2010, *MNRAS*, 408, 87
 Pilyugin L. S., Vílchez J. M., Thuan T. X., 2010, *ApJ*, 720, 1738
 Podsiadlowski Ph., Joss P. C., Hsu J. J. L., 1992, *ApJ*, 391, 246
 Prantzos N., Boissier S., 2003, *A&A*, 406, 259
 Prieto J. L., Stanek K. Z., Beacom J. F., 2008, *ApJ*, 673, 999
 Renzo M. et al., 2018, preprint (astro-ph:1804.09164R)
 Sana H. et al., 2012, *Science*, 337, 444
 Sana H. et al., 2014, *ApJS*, 215, 15
 Smartt S. J., 2015, *PASA*, 32, e016
 Stanway E. R., Eldridge J. J., Becker G. D., 2016, *MNRAS*, 456, 485
 Sukhbold T., Woosley S. E., 2014, *ApJ*, 783, 105
 Sánchez S. F. et al., 2016, *A&A*, 594, A36
 Van Bever J., Belkous H., Vanbeveren D., Van Rensbergen W., 1999, *New Astron.*, 4, 173
 van Dyk S. D., 1992, *AJ*, 103, 1788

- van Zee L., Haynes M. P., 2006, *ApJ*, 636, 214
 van Zee L., Salzer J. J., Haynes M. P., O'Donoghue A. A., Balonek T. J., 1998, *AJ*, 116, 2805
 Williams B. F., Hillis T. J., Murphy J. W., Gilbert K., Dalcanton J. J., Dolphin A. E., 2018, *ApJ*, 860, 39
 Williams B. F., Peterson S., Murphy J., Gilbert K., Dalcanton J. J., Dolphin A. E., Jennings Z. G., 2014, *ApJ*, 791, 105
 Woods T. E., Gilfanov M., 2016, *MNRAS*, 455, 1770
 Xiao L., Stanway E. R., Eldridge J. J., 2018, *MNRAS*, 477, 904
 Zapartas E. et al., 2017, *A&A*, 601, 29

SUPPORTING INFORMATION

Supplementary data are available at [MNRAS](https://www.mnras.org/) online.

Table A1. We give the best-fitting parameters for the no-leakage case, $\log(\text{age yr}^{-1})$, $\log(n_{\text{H}} \text{ cm}^{-3})$, $\log(U)$ and $12 + \log(\text{O}/\text{H})$, for each CCSN host H II region, from single-star and binary-star populations.

Table A2. We give the best-fitting parameters for the leakage case, $\log(\text{age yr}^{-1})$, $\log(n_{\text{H}} \text{ cm}^{-3})$, $\log(U)$ and $12 + \log(\text{O}/\text{H})$, for each CCSN host H II region, from single-star and binary-star populations.

Figure B1. Age distributions derived using the three methods for the sample of flux within 1 arcsec²: directly from the H α EW, best-fitting models without ionizing photon leakage and best-fitting models including leakage. The black bars denote single-star models and red (SNe II) and blue (SNe Ibc) bars denote binary-star models.

Figure B2. Age distributions derived using the three methods for the sample of flux from the nearest H II regions: directly from the H α EW, best-fitting models without ionizing photon leakage and best-fitting models including leakage. The black bars denote single-star models and red (SNe II) and blue (SNe Ibc) bars denote binary-star models.

Please note: Oxford University Press is not responsible for the content or functionality of any supporting materials supplied by the authors. Any queries (other than missing material) should be directed to the corresponding author for the article.

APPENDIX A: BEST-FITTING PARAMETERS FOR CCSN HOST H II REGIONS

Table A1. We give the best-fitting parameters for the no-leakage case, $\log(\text{age yr}^{-1})$, $\log(n_{\text{H}} \text{ cm}^{-3})$, $\log(U)$ and $12 + \log(\text{O}/\text{H})$, for each CCSN host H II region, from single-star and binary-star populations. The full table is available online.

SN name	SN type	Single-star models				Binary-star models			
		$\log(\text{age yr}^{-1})$	$\log(n_{\text{H}} \text{ cm}^{-3})$	$\log(U)$	$12 + \log(\text{O}/\text{H})$	$\log(\text{age yr}^{-1})$	$\log(n_{\text{H}} \text{ cm}^{-3})$	$\log(U)$	$12 + \log(\text{O}/\text{H})$
2000da	II	7 \pm 0	3 \pm 0	-1.77 \pm 0.27	8.41 \pm 0.08	7.6 \pm 0	1.26 \pm 0.86	-3.59 \pm 0.11	8.77 \pm 0.03
2016eob	II	7.1 \pm 0.21	3 \pm 0.11	-1.5 \pm 0.13	7.91 \pm 0.27	7.8 \pm 0.03	1.96 \pm 0.95	-3.41 \pm 0.1	8.72 \pm 0.1
2003ld	II	7 \pm 0.22	3 \pm 0.66	-1.51 \pm 0.26	8.21 \pm 0.22	7.42 \pm 0.05	2.24 \pm 1.02	-3.44 \pm 0.12	8.85 \pm 0.26
2005db	IIIn	8 \pm 0.22	3 \pm 0.11	-3.9 \pm 0.5	9.13 \pm 0.26	7.4 \pm 0	0.22 \pm 0.88	-3.78 \pm 0.14	8.77 \pm 0.15
1999ge	II	7.6 \pm 0.05	3 \pm 0.2	-1.63 \pm 0.16	8.07 \pm 0.23	7.98 \pm 0.05	2.91 \pm 0.23	-3.75 \pm 0.3	8.87 \pm 0.08
2017fqo	II	8 \pm 0.54	3 \pm 0	-1.5 \pm 0.72	8.52 \pm 0.26	7.76 \pm 0.05	2.92 \pm 0.57	-3.48 \pm 0.1	8.39 \pm 0.33
2006ee	IIIP	7.9 \pm 0.04	3 \pm 0.45	-1.5 \pm 0.24	9.13 \pm 0.24	8 \pm 0	3 \pm 0.22	-3.64 \pm 0.2	8.4 \pm 0.06
2011aq	II	7 \pm 0	3 \pm 0.24	-1.61 \pm 0.3	8.39 \pm 0.03	7.5 \pm 0	1.14 \pm 0.81	-3.35 \pm 0.1	8.78 \pm 0.06
2008ie	IIb	7.6 \pm 0.05	3 \pm 0.2	-1.58 \pm 0.11	8.63 \pm 0.3	8 \pm 0	2.93 \pm 0.33	-3 \pm 0.2	8.4 \pm 0.05
2009ie	IIIP	6.9 \pm 0.24	3 \pm 0.23	-2.69 \pm 0.33	8.52 \pm 0.05	7.5 \pm 0	0.83 \pm 0.76	-3.36 \pm 0.05	8.5 \pm 0.1

Table A2. We give the best-fitting parameters for the leakage case, $\log(\text{age yr}^{-1})$, $\log(n_{\text{H}} \text{ cm}^{-3})$, $\log(U)$ and $12 + \log(\text{O}/\text{H})$, for each CCSN host H II region, from single-star and binary-star populations. The full table is available online.

SN name	SN type	Single-star models				Binary-star models			
		$\log(\text{age yr}^{-1})$	$\log(n_{\text{H}} \text{ cm}^{-3})$	$\log(U)$	$12 + \log(\text{O}/\text{H})$	$\log(\text{age yr}^{-1})$	$\log(n_{\text{H}} \text{ cm}^{-3})$	$\log(U)$	$12 + \log(\text{O}/\text{H})$
2000da	II	6.28 ± 0.27	2.92 ± 0.40	-3.55 ± 0.07	8.75 ± 0.08	7.17 ± 0.15	1.12 ± 0.85	-3.63 ± 0.06	8.93 ± 0.00
2016eob	II	6.35 ± 0.25	2.73 ± 0.29	-3.34 ± 0.08	8.58 ± 0.10	7.23 ± 0.21	1.25 ± 0.80	-3.52 ± 0.06	8.79 ± 0.06
2003ld	II	6.10 ± 0.18	2.48 ± 0.92	-3.33 ± 0.04	8.47 ± 0.09	7.05 ± 0.12	1.14 ± 0.73	-3.33 ± 0.09	8.80 ± 0.07
2005db	IIIn	6.32 ± 0.28	2.94 ± 0.20	-3.61 ± 0.09	8.77 ± 0.00	7.15 ± 0.17	1.40 ± 1.04	-3.72 ± 0.08	8.98 ± 0.08
1999ge	II	6.63 ± 0.56	3.00 ± 0.00	-3.49 ± 0.25	8.86 ± 0.11	7.13 ± 0.07	1.81 ± 0.89	-3.06 ± 0.17	8.93 ± 0.00
2017fqo	II	6.00 ± 0.04	2.98 ± 0.22	-3.46 ± 0.09	8.36 ± 0.11	7.18 ± 0.07	2.91 ± 0.22	-3.63 ± 0.07	8.69 ± 0.16
2006ee	IIIP	6.00 ± 0.04	2.98 ± 0.20	-3.70 ± 0.11	8.34 ± 0.10	7.19 ± 0.07	2.97 ± 0.15	-3.81 ± 0.08	8.68 ± 0.15
2011aq	II	6.17 ± 0.23	2.89 ± 0.27	-3.32 ± 0.06	8.63 ± 0.09	7.10 ± 0.10	1.04 ± 0.69	-3.32 ± 0.07	8.87 ± 0.08
2008ie	IIb	7.20 ± 0.78	2.93 ± 0.18	-2.44 ± 0.77	8.99 ± 0.17	7.41 ± 0.29	2.48 ± 0.33	-3.40 ± 0.25	8.93 ± 0.00
2009ie	IIIP	6.03 ± 0.07	2.39 ± 0.90	-3.34 ± 0.07	8.39 ± 0.05	7.10 ± 0.06	0.85 ± 0.75	-3.40 ± 0.08	8.77 ± 0.00

APPENDIX B: CCSNE AGES BY VARYING H II REGION DEFINITION

In the main part of the paper, we identify the SN parent H II region as the stellar population present within a 1 kpc^2 projected region centred on the explosion site. This has the advantage of scaling with the distance (or redshift, and hence projected angular size) to the source. However, the IFU data from PISCO allow an alternative definition of the SNe host population.

Here, we complement the SNe age results as derived in the main part of the paper with estimates drawn from two differently defined samples. The first sample defines the SN host region as the observed flux detected within a fixed 1 arcsec^2 aperture centred at the SN location. This better approximates a fixed slit-width method from conventional spectroscopy, but results in a physical size that depends on the redshift. The second sample identifies the nearest H II region to the explosion site and extracts the flux associated with it, rather than centring on the explosion site.

We apply the same method discussed in Sections 3 and 4 to these two alternatively derived samples in order to estimate the SNe ages from the properties of their nebular emission. Figs B1 and B2 (see the supporting information) show the age distribution for regions within 1 arcsec^2 and for the nearest H II region sample separately. We obtain similar results as those presented in Fig. 15, which suggests that our main results and their interpretation are not highly sensitive to the definition of the host population, as long as this is sufficiently representative of stars near the explosion site.

This paper has been typeset from a \LaTeX file prepared by the author.